Integrated Arctic Observation System

Research and Innovation Action under EC Horizon2020

Grant Agreement no. 727890

Project coordinator:

Nansen Environmental and Remote Sensing Center, Norway

Deliverable 6.17

Ice discharge from glaciers to the ocean

Model-based demonstration of calculations of ice discharge from selected glaciers to the ocean, aimed to predict the contribution of glaciers to sea level rise

Start date of project:	01 December 2016	Duration:	60 months
Due date of deliverable:	30 September 2021	Actual submission date:	29 September 2021
Lead beneficiary for preparing the deliverable:		UPM	
Person-months used to produce deliverable:		16.5 pm	

Authors: Francisco Navarro, Eva De Andrés, Kenneth Mankoff, Marina González, Jaime Otero, María Isabel de Corcuera, Javier Lapazaran

Version	DATE	CHANGE RECORDS	LEAD AUTHOR
1.0	14.12.2016	Template	L. H. Pettersson
1.1	19.05.2021	1st Draft	F. Navarro
1.2	15.06.2021	GEUS contributions	K. Mankoff
1.3	11.07.2021	UPM contributions	E. De Andrés
2.0	06.09.2021	2nd draft	F. Navarro
2.1	22.09.2021	3rd draft for internal review	F. Navarro
2.2	25.09.2021	Revisions by Anne Solgaard included for external review	F. Navarro
2.3	26.09.2021	Revisions by Michael Zemp (WGMS) and Magnús Magnússon (IGS) included for technical review	F. Navarro
3.0	27.09.2021	Technical revisions by Kjetil Lygre included	F. Navarro
3.1	29.09.2021	Final technical review and submission	K. Lygre

Approval	Date:	Sign.
X	29 September 2021	Coordinator

USED PERSON-MONTHS FOR THIS DELIVERABLE					
No	***Beneficiary***	***PM***	***No***	***Beneficiary***	***PM***
1	NERSC		24	TDUE	
2	UiB		25	GINR	
3	IMR		48	UNEXE	
4	MISU		27	NIVA	
5	AWI		28	CNRS	
6	IOPAN		29	U Helsinki	
7	DTU		30	GFZ	
8	AU		31	ARMINES	
9	GEUS	6.0	32	IGPAN	
10	FMI		33	U SLASKI	
11	UNIS		34	BSC	
12	NORDECO		35	DNV GL	
13	SMHI		36	RIHMI-WDC	
14	USFD		37	NIERSC	
15	NUIM		38	WHOI	
16	IFREMER		39	SIO	
17	MPG		40	UAF	
18	EUROGOOS		41	U Laval	
19	EUROCEAN		42	ONC	
20	**UPM**	**10.6**	43	NMEFC	
21	UB		44	RADI	
22	UHAM		45	KOPRI	
23	NORCE		46	NIPR	
			47	PRIC	

DISSEMINATION LEVEL		
PU	Public, fully open	**X**
CO	Confidential, restricted under conditions set out in Model Grant Agreement	
CI	Classified, information as referred to in Commission Decision 2001/844/EC	

EXECUTIVE SUMMARY

This document, Deliverable 6.17 - Ice discharge from glaciers to the ocean: Model-based demonstration of calculations of ice discharge from selected glaciers to the ocean, aimed to predict the contribution of glaciers to sea level rise, has been carried out as part of Task 6.4-Natural hazards in the Arctic. This deliverable describes a modelling-based approach developed by Universidad Politécnica de Madrid (UPM) to quantify the partitioning of solid ice discharge into its two main components, namely iceberg calving and submarine melting. For Greenlandic glaciers, it can take advantage of using, as part of its input data, those produced by the freshwater runoff product developed by the Geological Survey of Greenland and Denmark (GEUS), and the modelling-based estimates of solid ice discharge (obtained as sum of iceberg calving and submarine melting) can be validated against those produced by the solid ice discharge product developed by GEUS.

This deliverable is conceived as a demonstration to stakeholders, who, in our case, are primarily researchers interested in estimating the current contribution of glacier wastage to sea-level rise and the future projections of such contributions under various scenarios of greenhouse gasses emissions. The demonstration is based on a video (ca. 20 min.) available through the INTAROS YouTube channel and the education material available though the INTAROS website. There is also a shorter version (a trailer, ca. 4 min.) of the video, aimed to provide an overview of the contents of the longer version.

This written report provides a more detailed account of the coupled glacier dynamics-fjord circulation model in which the procedure for partitioning the ice discharge into its main components is based. Alternatively, there is a simpler version of the model, which is a coupled glacier dynamics-buoyant plume model that greatly reduces the computation time, while still providing sufficiently accurate results. The glacier dynamics model is defined by the Stokes system of partial differential equations, an associated constitutive relationship, together with an iceberg calving model, and is solved using the finite-element ELMER/Ice code. The fjord circulation (and submarine melting) model is defined by Boussinesq form of the Navier-Stokes equation set, plus the Holland and Jenkins equations defining the thermodynamic equilibrium at the fjord-glacier front interface and is solved using the finite-volume MITgcm code. The plume parameterisation model that replaces the fjord circulation model in the simplified version of the coupled model is programmed using MATLAB.

Table of Contents

1. Introduction 5
1.1. Motivation and aims. Stakeholder needs 5
1.2. Whom is this deliverable addressed to? 7
1.3. Structure of the document 7
2. Demonstration of calculation of ice discharge to the ocean 8
2.1. Observation-based ice discharge calculations 8
2.1.1. Solid ice discharge 8

2.1.2. Freshwater runoff 9

2.2. Model-based ice discharge calculations. Partitioning of ice discharge into iceberg calving and submarine melting 10

2.2.1. Building the glacier-fjord and glacier-plume coupled models: components, governing equations and set up 10

COMPONENT 1: THE GLACIER DYNAMICS MODEL (Otero et al., 2017) 11

Dynamical model equations and flow law 11

Continuum damage mechanics model 12

Free surface evolution and Boundary conditions 12

Calving model 13

Numerical solution 13

COMPONENT 2: THE FJORD CIRCULATION MODEL (De Andrés et al., 2018) 14

Mathematical formulation of fjord circulation 15

Numerical modelling: MITgcm 17

How to run the fjord model 17

Model set up and calibration 18

COMPONENT 3: THE SUBMARINE MELT MODEL 22

COMPONENT 4: THE LINE PLUME MODEL (De Andrés et al., 2020, 2021) 23

Mathematical formulation of buoyant line-plumes 23

Numerical modelling and calibration 24

COUPLING THE ICE-OCEAN MODEL COMPONENTS 26

2.2.2. Partitioning into calving and submarine melting using the coupled models. A case study for Hansbreen-Hansbukta glacier-fjord system 29

PHYSICAL SETTINGS & DATA 29

EVALUATION OF THE COUPLED MODELS' PERFORMANCE 31

Submarine melting 31

Front position 32

ICE DISCHARGE PARTITIONING: SUBMARINE MELTING + CALVING 35

3. Synthesis on achievements concerning stakeholder needs and data gaps 36

4. Outlook and recommendations for roadmap 37

5. Summary 38

Literature 40

1. Introduction

This section describes the motivation and aims of the work carried out within INTAROS Task 6.4 using data and methods available from the iAOS, aiming to give a response to the stakeholder needs.

1.1. Motivation and aims. Stakeholder needs

Mass losses from glaciers and ice caps (henceforth, glaciers) are projected to account for 79 to 157 mm of global mean sea−level rise (SLR) to the end of the 21st century, depending on the emission scenario (Huss and Hock, 2015). Between 10 and 30% of these losses correspond to frontal ablation, dominated by calving and submarine melting in regions such as peripheral Antarctica, Svalbard and the Russian Arctic (Huss and Hock, 2015; Hanna et al., 2020). Although the global glacier volume is only ~ 0.6% of the ice sheet volume (Greenland and Antarctica), current glacier contribution to SLR is close to that of the ice sheets (IPCC, 2019), primarily due to the high sensitivity of glaciers to atmospheric and oceanic forcing (Rignot et al., 2010; Motyka et al., 2013; Straneo and Heimbach, 2013; Luckman et al., 2015; Holmes et al., 2019). The Greenland ice sheet (GrIS) is another important contributor to SLR, currently at a pace roughly twice that of the Antarctic ice sheet (IPCC, 2019). About 60% of the GrIS mass loss is attributed to negative surface mass balance from surface melt and runoff at the lower-altitude zones at the margins, and the remaining 40% to solid ice discharge from marine-terminating glaciers (Csatho et al., 2014; Enderlin et al., 2014; van den Broeke et al., 2016).

Beyond the SLR issue, the freshwater input from glacier wastage generates considerable changes in fjord stratification (De Andrés et al., 2020) and sediment distribution (Mugford and Dowdeswell, 2011; Overeem et al., 2017), affecting surrounding marine ecosystems (Meire et al., 2017; Oliver et al., 2018; Hopwood et al., 2018), atmospheric CO_2 intakes (Meire et al., 2015) and regional ocean circulation (Bamber et al., 2018; Oliver et al., 2018). Thus, studying processes occurring at the glacier−fjord interface is key to understand ongoing changes and to generate future projections.

In the Arctic region, frontal ablation in an important component of the glacier and ice-sheet mass losses (Huss and Hock, 2015). As the main components of frontal ablation (iceberg calving and submarine melting) are difficult to evaluate separately, frontal ablation is often approximated by the solid ice discharge through flux gates close to the calving front (Fig. 2.1.1 below). This approximation is valid as far as there are no glacier front position changes. Otherwise, a correction term accounting for such changes has to be introduced. Additionally, if the flux gate is not sufficiently close to the glacier front, a further correction must be applied to account for the surface mass balance between the flux gate and the calving front.

The submarine melting at the glacier front (or below the floating ice tongues or ice shelves, which are very scarce in Artic glaciers) is strongly influenced by the subglacial discharge at the glacier front of surface meltwaters that reach the glacier bed through crevasses and moulins. Therefore, the estimation of solid ice discharge and of freshwater runoff are essential for calculating the mass balance of glaciers and ice sheets. On the other hand, being able to estimate the partitioning of solid ice discharge into its two main components (iceberg calving and submarine melting) is fundamental to support the projections of glacier mass losses and its contribution to sea-level rise (e.g., Edwards et al., 2021).

Finally, we note that frontal ablation estimates can be validated by subtracting from the geodetic mass balance estimates (which provide the total mass balance of the ice masses under investigation) the surface mass balance (and the basal mass balance, wherever relevant). The recent availability of glacier geodetic mass balance observations at global (planetary) scale, such as those by Hugonnet et al. (2021), and the availability of such estimates, as well as many at the regional scale, at databases such as the Fluctuation of Glacier database hosted by the World Glacier Monitoring Service (WGMS, 2021a), which also stores the world-wide collection of glacier surface mass observations, opens the door to further studies allowing the validation of the results obtained by using independent methods and data sources. Furthermore, the use of these geodetic methods provides directly SLR contributions (except for a correction to account for the change of the fraction of the glacier already below sea level), without requiring estimates for calving and submarine melting (e.g., Zemp et al., 2019).

The above summarizes the main stakeholder needs in the context of this deliverable and motivates the focus of the deliverable, which has been conceived as a demonstration for stakeholders aiming:

1) To present two useful data tools developed by the Geological Survey of Denmark and Greenland (GEUS) to estimate the solid ice discharge and the freshwater runoff from the whole of the Greenland ice sheet or its individual basins. This is the focus of Section 2.1.

2) To show a modelling-based procedure, developed by Universidad Politécnica de Madrid (UPM), allowing to estimate the partitioning of solid ice discharge into its two main components (iceberg calving and submarine melting). This is the focus of Section 2.2.

The demonstration is based on a video available through the INTAROS YouTube channel and the education material available though the INTAROS website (http://intaros.eu/). There is a longer version of the video (ca. 20 min.) and a shorter one (a trailer, ca. 4 min.) aimed to give a brief overview of the contents of the longer version. This written report is aimed to provide supporting material to the contents of the video demonstration. In particular, getting a deep understanding of the modelling-based approach to calculate the partitioning of the solid ice discharge into its two main components is facilitated by the supporting material presented in Section 2.2.

1.2. Whom is this deliverable addressed to?

The above aims are a direct response to the stakeholders needs described in the motivation. In our case, the stakeholders are: 1) the scientists interested in the estimates of the mass losses from the Arctic glaciers and the Greenland ice sheet and their contribution to sea-level rise; 2) the scientists interested in the projections of mass losses from glaciers and ice sheets, for which understanding the partitioning of ice discharge into iceberg calving and submarine melting is key to well-founded forecasts. The deliverable can also be useful to researchers wishing to understand the physical processes behind the mentioned partitioning of solid ice discharge. In this way, this deliverable is mostly addressed to researchers. While Section 2.1 (and its corresponding part in the video) describes some tools that can be useful to end users, as the GEUS ice discharge and freshwater runoff products are *end products*, Section 2.2 (and its corresponding part in the video) describe a rather complex *modelling-based procedure* to split ice discharge into iceberg calving and submarine melting. Although any user with a Earth-science background and a basic mathematical background can easily follow the video and understand the basics of how the modelling-based procedure works, following all of the details of the procedure (as given in the present report), and applying it for glacier-fjord systems other than that presented as example in the report require some additional skills in numerical modelling and computing.

Of course, the results compiled by scientists using the GEUS tools and/or by applying the UPM procedure (e.g. on contributions of glacier/ice-sheet wastage to sea-level rise) can then be useful to other end users, such as coastal planners of policy makers. But this deliverable, in its original form, is mostly addressed to researchers in the field of Earth sciences.

1.3. Structure of the document

This document is structured as follows:

- Chapter 1 contains an introduction, which first motivates the work done and introduces its scientific background, from which the stakeholder needs naturally arise, as well as the deliverable aims addressed to satisfy such needs. It also includes a brief account of the stakeholders to which this demonstration-based deliverable is addressed.
- Chapter 2 is the bulk of the deliverable and contains an account of both the solid ice discharge and the freshwater runoff data products developed by GEUS (Section 2.1) and a detailed account of the modelling-based approach developed by UPM to separate the solid ice discharge into iceberg calving and submarine melting (Section 2.2). This provides also support material to the accompanying video demonstration on which this deliverable strongly relies.
- Chapter 3 summarizes how the above-mentioned data and modelling tools satisfy the stakeholder needs stated in Chapter 2 and describes the data and modelling gaps.
- Chapter 4 provides some outlook and presents some recommendations for roadmap, mostly aimed to fill the gaps outlined in Chapter 3.
- Chapter 5, finally, is a summary of this report with emphasis on its relation to other work packages (WPs) and tasks within the INTAROS project.

2. Demonstration of calculation of ice discharge to the ocean

2.1. Observation-based ice discharge calculations

Contributors: Kenneth Mankoff.

The total volume of freshwater from Greenlandic marine-terminating glaciers into the ocean comes from two sources: Ice discharge and freshwater discharge. Ice discharge is divided at the ice/ocean boundary into solid ice discharge (i.e., iceberg calving) and submarine melt. Freshwater discharge is the liquid water from the ice sheet surface melted far upstream that flows out either from streams that enter the fjords, or subglacially at the base of marine terminating glaciers.

Submarine melt is controlled by 1) the temperature of the fjord water especially at the bottom, and 2) the amount of subglacial freshwater discharge flowing out at the base of the glacier. Submarine melt is discussed further in Section 2.2. Here we address 1) the total ice discharge across flux gates upstream of the terminus – that is, the sum of iceberg calving and submarine melt, and 2) the subglacial component of the freshwater discharge.

2.1.1. Solid ice discharge

We have created a high spatial (glacier scale) and temporal (bi-weekly) estimate of where and when solid ice and submarine melt (combined) discharges into the surrounding fjords and seas. This is an "operational" product from 1968 until last month, updating approximately every 12 days with a one-month lag. Discharge is provided for every marine terminating outlet glacier. The product is described in detail in Mankoff et al. (2020a) and is available through the INTAROS data portal and the GEUS dataverse repository (https://dataverse01.geus.dk/dataverse/ice_discharge).

Inputs to this product are ice sheet surface velocity, both from MeaSURes (Howat 2017; Joughin 2018; Joughin et al. 2010; Joughin et al. 2018) and the PROMICE Sentinel Ice Velocity product (Solgaard et al., 2021), and the BedMachine dataset (Morlighem et al., 2017) for ice thickness. From these two properties (velocity and thickness), ice volume flow rate across flux gates is computed as velocity times ice thickness times gate width times ice density (Fig. 2.1.1).

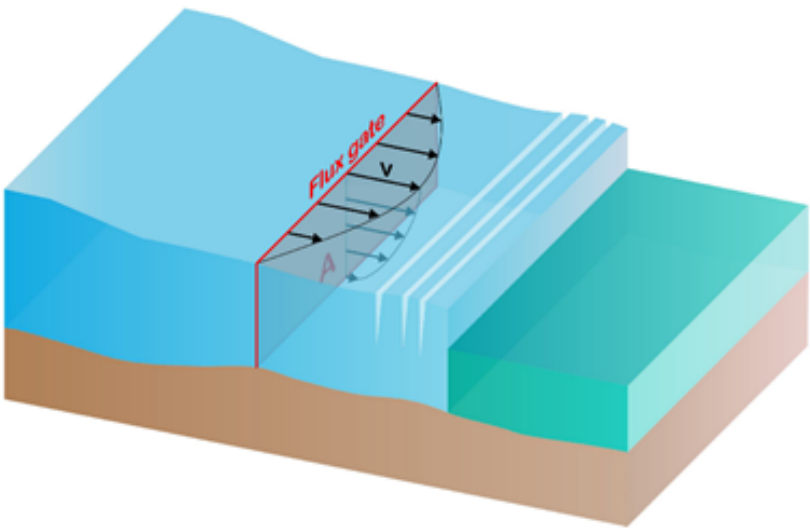

Figure 2.1.1 Solid ice discharge through a flux gate.

Time series are provided for individual glaciers (Fig. 2.1.2), sectors and regions, and the entire Greenland ice sheet. Errors in ice discharge can be estimated, from those of its individual components, following the procedure described in Sánchez-Gámez and Navarro (2018).

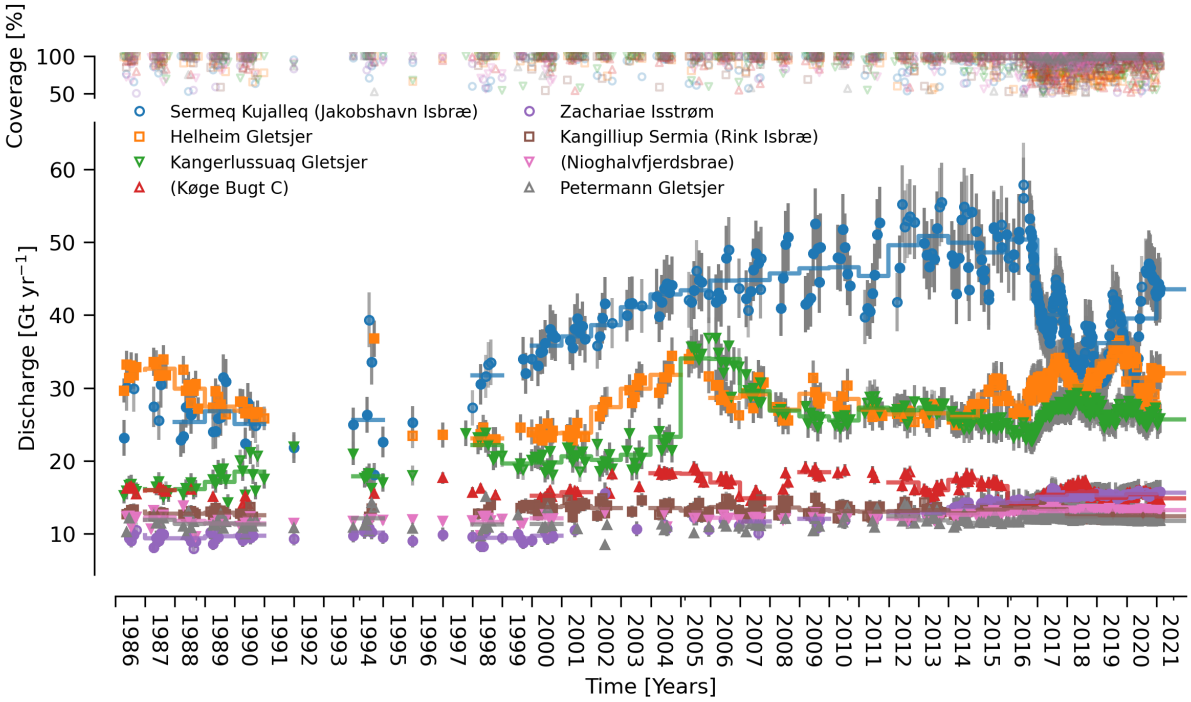

Figure 2.1.2 Discharge time series for eight major glaciers.

2.1.2. Freshwater runoff

In addition to ice discharge (which is the sum of iceberg discharge and submarine melt) we provide a dataset of freshwater runoff. The subglacial component of this runoff a key driver of the submarine melt portion of the ice discharge (Mankoff et al., 2016; De Andrés et al., 2018). We have created a high spatial (outlet scale) and temporal (daily) estimate of where and when liquid freshwater (i.e., rainfall, melted ice, and melted snow) discharges into the surrounding fjords and seas from 1958 through 2019. This product is generated from the HIRHAM (Langen et al., 2017) and MAR (Fettweis et al., 2020) RCMs and the ArcticDEM surface topography (Porter et al., 2018). Land runoff is routed using traditional topographic routing techniques. Subglacial meltwater is assumed to penetrate to the bed within the grid cell where it is generated and is routed instantaneously to the coastal outlet using traditional subglacial routing techniques, assuming the subglacial pressure is equal to the pressure of the overhead ice. The freshwater product is described in Mankoff et al. (2020b) and it can be accessed through the INTAROS data portal and is stored in the GEUS Dataverse repository (https://dataverse01.geus.dk/dataverse/freshwater). An example of freshwater discharge product is shown in Figure 2.1.3.

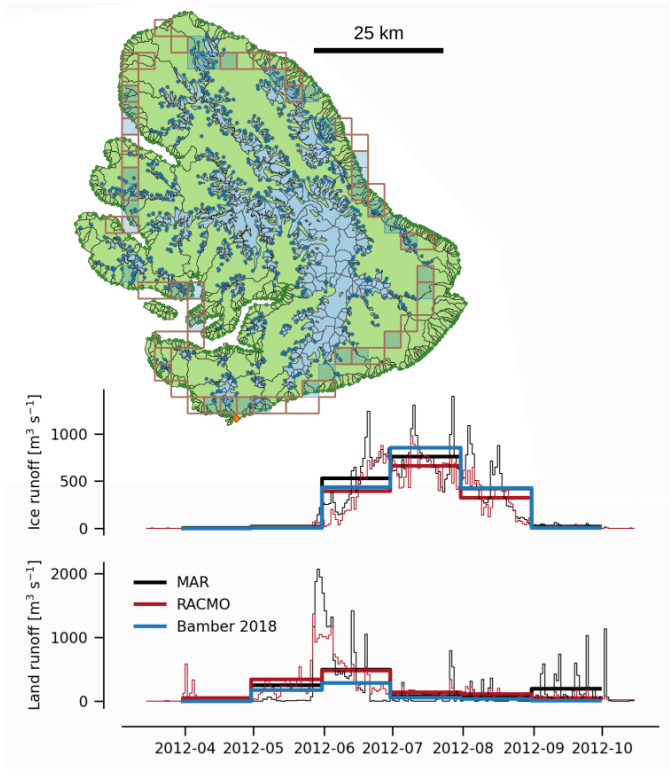

Figure 2.1.3 Example of freshwater discharge product. 100 m ice basins (blue lines) and outlets (blue dots) and land basins and outlets (green lines and dots respectively) cover Disko Island. Each outlet has a runoff time series, but the entire island runoff (summed) is shown below for ice (upper graph) and land (lower graph).

2.2. Model-based ice discharge calculations. Partitioning of ice discharge into iceberg calving and submarine melting

Contributors: Francisco Navarro, Eva De Andrés, Marina González, Jaime Otero, María Isabel de Corcuera, Javier Lapazaran.

2.2.1. Building the glacier-fjord and glacier-plume coupled models: components, governing equations and set up

The first step is to get a clear view of the system and its components (Fig. 2.2.1). On one side, we have the glacier, which, although made of water in solid state, can be physically treated as a super-viscous fluid. On the other side, we have the fjord, which is the water component of the system and encompasses a combination of both laminar and turbulent flow dynamics. In our glacier-fjord system, the turbulent regime will be mostly due to the high-energy inputs of subglacial meltwater discharges, which generate turbulent ascent plumes attached to the submerged icefront face. The initial approach includes the complete fjord circulation, and the second approach parameterizes the turbulent plume to decrease the time of computation. The interface between the glacier and the fjord (or plume) components is where submarine melting occurs, depending on and affecting both glacier and fjord (plume) dynamics. Therefore, four different sets of equations are considered (one for each component): the glacier, the fjord, the buoyant plume and the submarine melting.

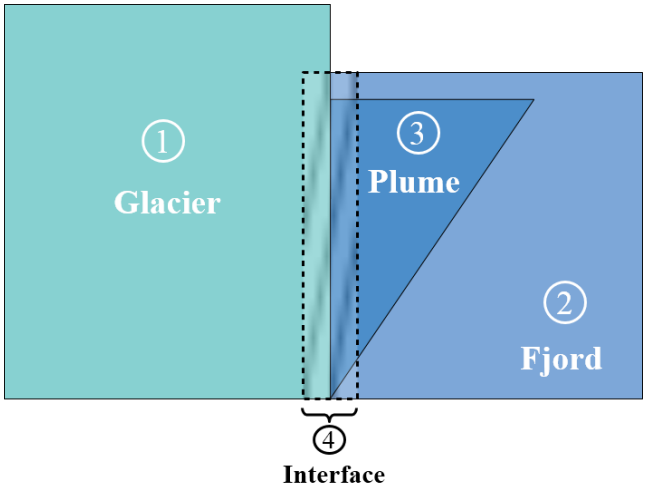

Figure 2.2.1 Schematics of the different components of the system.

To solve the equations governing the system dynamics, the solutions of each component of the system are approximated by different numerical discretizations. Three approaches, *finite elements*, *volumes* and *differences*, are used to solve the glacier, fjord and plume components, respectively. These are implemented using ELMER/Ice, MITgcm and Matlab software packages. ELMER/Ice and MITgcm will be configured to suit our physical problem, domain geometry and boundary conditions, while a Matlab routine will be developed to solve the plume model parameterization.

The submarine melt model (interface in Fig. 2.2.1) is used in both the fjord and the plume model as boundary conditions to close the set of equations. Computed melt rates of the glacier front are incorporated into the glacier dynamics model by reshaping its domain through a modified glacier geometry.

COMPONENT 1: THE GLACIER DYNAMICS MODEL (Otero et al., 2017)

Dynamical model equations and flow law

Ice is treated as an incompressible, continuous and highly viscous fluid. The dynamical model is described by the Stokes system of equations, describing the conservation of linear momentum and mass:

$$\nabla \cdot \boldsymbol{\sigma} + \rho_i \boldsymbol{g} + \boldsymbol{F} = \boldsymbol{0}, \qquad (2.1)$$
$$\nabla \cdot \boldsymbol{u} = 0,$$

where $\boldsymbol{\sigma}$ is the Cauchy stress tensor, $\boldsymbol{u}$ is the velocity vector, $\boldsymbol{g}$ is the gravity acceleration vector and ρ_i is the ice density. A body force $\boldsymbol{F}$ is added to account for the lateral friction in our 2D model. The shape factor (Nye, 1965) is here extended to the full-Stokes formulation by defining the body force $\boldsymbol{F}$ as (Jay-Allemand et al., 2011):

$$\boldsymbol{F} = -\rho_i \boldsymbol{g} \cdot \boldsymbol{t}(1 - f_s)\boldsymbol{t} \qquad (2.2)$$

where $\boldsymbol{t}$ is the unit vector tangent to the top surface and the shape factor f_s can be estimated from a scalar function of the glacier's transversal shape (Jay-Allemand et al., 2011), such that:

$$f_s = \frac{2}{\pi}\tan^{-1}\left(\frac{0.186 w_h}{h_i}\right)^{-1}, \tag{2. 3}$$

where the ice thickness is given by the difference between the surface and bed elevations, $h_i(x) = z_s(x) - z_b(x)$, and $w_h(x)$ is the half-width at the glacier surface.

We adopt Nye's generalization of Glen's flow law (Glen, 1955; Nye, 1957) as the constitutive relation, which links the deviatoric stress $\boldsymbol{\tau}$ to the strain rate $\dot{\boldsymbol{\varepsilon}}$:

$$\boldsymbol{\tau} = 2\eta\dot{\boldsymbol{\varepsilon}} \tag{2. 4}$$

The effective viscosity η is written as

$$\eta = \frac{1}{2}(EA_i)^{-1/n} I_{\dot{\varepsilon}_2}^{(1-n)/n} \tag{2. 5}$$

where $I_{\dot{\varepsilon}_2}$ represents the second invariant of the strain rate tensor, A_i is the softness parameter in Glen's flow law and E is an enhancement factor. We use typical values of $n = 3$ and $A_i = 0.1\ \mathrm{bar}^{-3}\mathrm{a}^{-1}$ (Cuffey and Paterson, 2010; Vieli et al., 2002).

Cauchy and deviatoric stresses are linked through the equation

$$\boldsymbol{\sigma} = \boldsymbol{\tau} - p\mathbf{I}, \qquad p = -\mathrm{tr}(\boldsymbol{\sigma})/3, \tag{2. 6}$$

where p is the local pressure (i.e., compressive mean stress) and $\mathbf{I}$ is the identity matrix.

Continuum damage mechanics model

The fracture-induced softening accounts for the loss of load-bearing surface area due to fractures under a scalar damage variable D. The enhancement factor E can be linked to the damage D (Borstad et al., 2012; Krug et al., 2014) as

$$E = \frac{1}{(1-D)^n} \tag{2. 7}$$

For undamaged ice ($D = 0$), $E = 1$ and the flow regime is unchanged. As damage increases ($D > 0$), $E > 1$, ice viscosity decreases, and flow velocity increases.

In this thesis, we assume that D is nonzero within the 2 km closest to the glacier front, linearly increasing towards the terminus, where it reaches a maximum value of 0.4 (Krug et al., 2015).

Free surface evolution and Boundary conditions

The time evolution of the glacier free surface is governed by

$$\frac{\partial z_S}{\partial t} = b_n - u_S\frac{\partial z_S}{\partial x} + w_S, \tag{2. 8}$$

where z_S is the surface elevation, t is time, u_S and w_S are the horizontal and vertical components of the flow velocity at the surface, respectively, and b_n is the surface mass balance.

The upper surface of the glacier is a traction-free zone with unconstrained velocities. At the ice divide at the head of the glacier, horizontal velocity and shear stresses are set to zero (Fig. 2.2.2).

For boundary conditions at the bed, we use a friction law that proportionally relates the sliding velocity (u_t) to the basal shear stress (σ_{nt}):

$$Cu_t = \sigma_{nt}, \tag{2. 9}$$

where the friction coefficient C is determined using the inverse Robin method described in Arthern and Gudmundsson (2010) and Jay-Allemand et al. (2011), which evaluates the mismatch between observed and modelled surface velocities by using a cost function. Every four-week period we calculate a continuous function for the surface velocity using a sixth-degree polynomial regression to be used in the inversion procedure.

At the glacier terminus, we set back stress (normal stress) to zero above sea level and equal to the water-depth-dependent hydrostatic pressure below sea level (see Otero et al., 2017).

Calving model

Calving is assumed to be triggered by the downward propagation of transverse surface crevasses near the calving front as a result of the extensional stress regime (Benn et al., 2007). The depth reached by a crevasse is that where the longitudinal tensile strain rate tending to open the crevasse equals the creep closure resulting from the ice overburden pressure (Nye, 1957; Todd and Christoffersen, 2014). The "net stress" σ_n can then be calculated as

$$\sigma_n = 2\tau_e \mathrm{sign}(\tau_{xx}) - \rho_i g d + P_w, \tag{2. 10}$$

which is considered positive for extension and negative for compression. The first term on the right-hand side of Eq. 2.10 represents the opening force of longitudinal stretching (Otero et al., 2010); τ_e represents the effective stress ($\tau_e^2 = \tau_{xx}^2 + \tau_{zx}^2$) and is multiplied by the sign function of the longitudinal deviatoric stress, τ_{xx}, to ensure that crevasse opening is only produced under longitudinal extension ($\tau_{xx} > 0$). The second term on the right-hand side is the ice overburden pressure, which leads to creep closure, where d is the crevasse depth. The last term represents the pressure exerted by the water filling the crevasse, which contributes to open the crevasse. Calving takes place when surface crevasses reach the sea level.

Numerical solution

The glacier is divided each time step into a quadrilateral mesh with 10 vertical layers and a horizontal grid size of ~50 m in the upper glacier and ~25 m near the terminus. The Stokes system of Eqns. 2.1 is solved by a finite element method using Elmer/Ice (Gagliardini et al., 2013) and the 2D stress and velocity fields are computed along the central flowline (Fig. 2.2.2). The new surface elevations are computed, using the free-surface evolution equation, from the surface mass-balance input and the surface velocities produced by the flow model and the grid nodes are shifted vertically to fit the new glacier geometry (for further details see Otero et al. (2017).

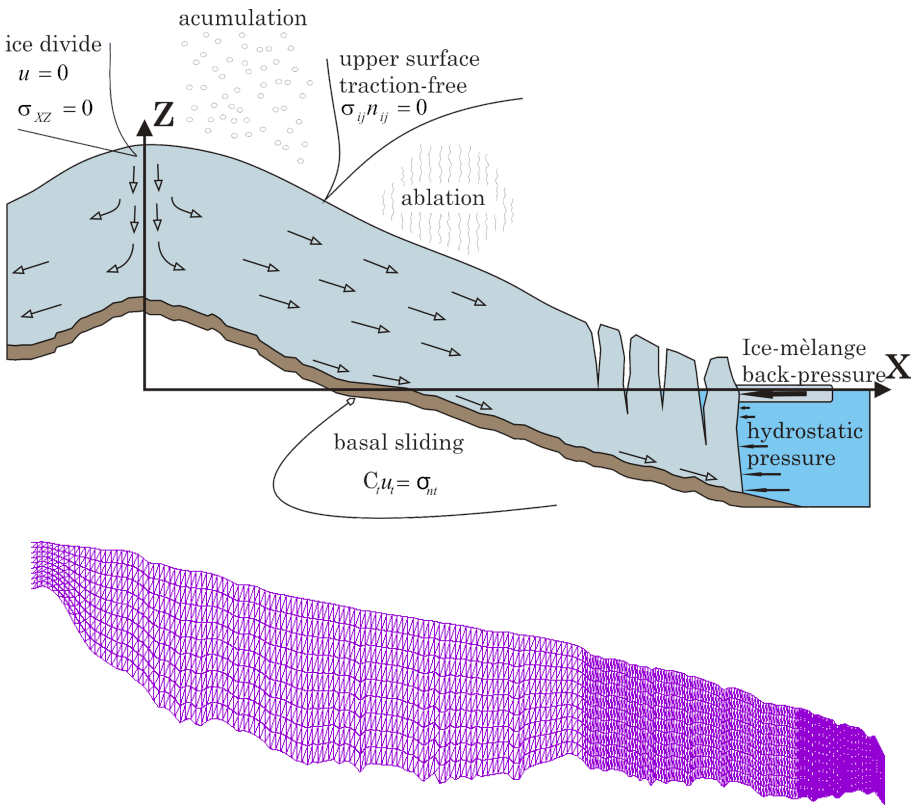

Figure 2.2.2 Schematics of the glacier-calving model and its domain mesh (from Otero et al. (2017).

At the terminus, the grid nodes are shifted down-glacier according to the velocity vector and the length of the time step, and the terminus position is then updated according to the calving criterion used.

Every four weeks (four time steps), we estimate the best-fit friction coefficient (Eq. 2.9) to be used for these four model runs. The choice of the initialization time step was made as a compromise between the time resolution needed for capturing the sudden changes in velocity and an acceptable computational cost.

COMPONENT 2: THE FJORD CIRCULATION MODEL (De Andrés et al., 2018)

The water movement inside a given fjord is the result of different processes, such as thermohaline instabilities, convection-driven circulation due to meltwater discharges, pressure gradients, wind advection or tidal currents (Fig. 2.2.3). The equations governing the fjord water circulation and the numerical methods used to solve them are detailed below.

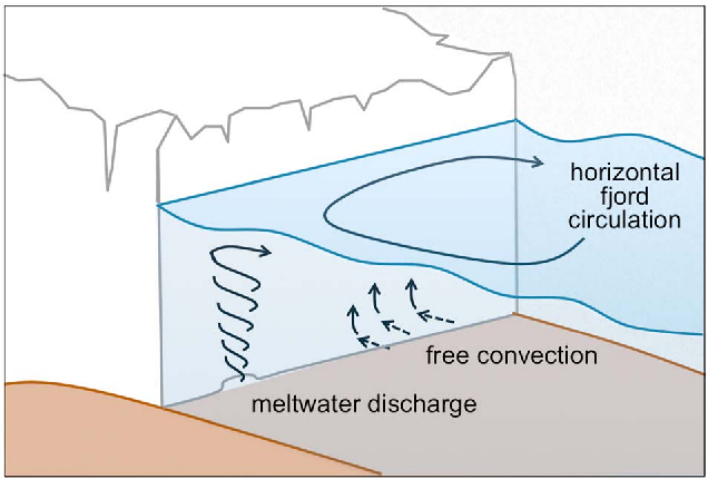

Figure 2.2.3 Schematics of fjord circulation processes (from Schild et al., 2018).

Mathematical formulation of fjord circulation

The equations governing the 2D motion of an incompressible stratified fluid in a rotating system are described here. Given that the dimension of our considered fjord domain will be much smaller than the Earth's radius, the subsequent equations assume a Cartesian system of $x - z$ coordinates.

Water density in the ocean is a complex function of temperature, salinity and pressure, $\rho(T, S, p)$, which can be found in Jackett and Mcdougall (1995). However, for most applications water density can be assumed as linearly dependent upon both temperature and salinity, such that

$$\rho = \rho_0[1 - \alpha_T(T - T_0) + \beta_S(S - S_0)], \tag{2. 11}$$

where $\rho_0 = 1028$ kg m^{-3} is the reference density for $T_0 = 10$ ºC and $S_0 = 35$ psu. α_T and β_S are the coefficients of thermal expansion and saline contraction of water, taking the values of 1.7 × 10^{-4} K^{-1} and 7.6 × 10^{-4}, respectively. Although in our fjord model we use the comprehensive density equation described in Jackett and Mcdougall (1995), it is reasonable to leave Eq. 2.11 within the text of this report to understand the effect that both T and S exert on water density.

One of the first statements in fluid mechanics is that mass must be conserved. Thus, any imbalance between convergence and divergence must create a local compression or expansion of the fluid. The material derivative of mass per unit volume (i.e., density, ρ) must therefore equal zero to ensure conservation of mass:

$$\frac{d\rho}{dt} = \frac{\partial \rho}{\partial t} + \frac{\partial}{\partial x}(\rho u) + \frac{\partial}{\partial z}(\rho w) = 0, \tag{2. 12}$$

where t is time and u and w are the horizontal and vertical components of the velocity vector, respectively. Armed with the *Boussinesq Approximation*, by which ocean density variations, ρ', (caused by the existing stratification and/or fluid motion) are small (< 3%) compared with the reference value ρ_0

$$\rho = \rho_0 + \rho'(x, z, t) \quad \text{with} \quad |\rho'| \ll \rho_0, \tag{2. 13}$$

we can simplify (2.12) to obtain

$$\frac{\partial u}{\partial x} + \frac{\partial w}{\partial z} = 0. \tag{2. 14}$$

This is the so-called continuity equation for incompressible fluids, which physically means that conservation of mass has become conservation of volume.

The conservation of linear momentum is expressed here in terms of the two components (horizontal and vertical) of the velocity vector:

$$\frac{du}{dt} - f_* w = -\frac{1}{\rho_0}\frac{\partial p}{\partial x} + A_{h,v}\nabla^2 u, \tag{2. 15}$$

$$\frac{dw}{dt} - f_* u = -\frac{1}{\rho_0}\frac{\partial p}{\partial z} - \frac{1}{\rho_0}\rho g + A_{h,v}\nabla^2 w. \tag{2. 16}$$

In Eqs. (2.15) and (2.16), all forces are expressed per unit volume. The terms on the left-hand side show the acceleration of a fluid particle as it moves along with the flow, which can be partitioned into the local time rate of change ($\frac{\partial}{\partial t}$) and the advective terms ($u\frac{\partial}{\partial x} + w\frac{\partial}{\partial z}$) for both velocity components u and w. f_* is the reciprocal Coriolis parameter for inertial reference systems ($f_* = 2\Omega\cos\varphi$), dependent on the angular frequency of Earth's rotation (Ω) and on the latitude (φ). Note that we do not include here the Coriolis f-parameter, since the velocity along the y-dimension is not considered in our 2D model. The right-hand side terms represent the effects of pressure, gravity (second term in Eq. 2.16) and viscous stress, where $A_{h,v}$ accounts for the horizontal and vertical kinematic-viscosity coefficient (quotient of dynamic viscous coefficient over density). These viscous coefficients might vary depending on the processes to be studied, so they must be properly adjusted in the model.

We consider the elevation of the sea surface (h) as a free boundary that evolves in time and space according to

$$\frac{\partial h}{\partial t} + H\frac{\partial \bar{u}^H}{\partial x} = 0, \tag{2. 17}$$

where H is the initial and local water depth. $\bar{u}^H$ accounts for the vertically averaged horizontal velocity ($\bar{u}^H = \frac{1}{H}\int_{-H}^{0} u(z)dz$) and evolves according to the momentum equations 2.15 and 2.16.

The heat and salt budgets are calculated by virtue of equations 2.18 and 2.19, respectively, which express the time evolution of T and S, accounting for advective (part of the material derivative in the left-hand side) and diffusive (right-hand side) processes:

$$\frac{dT}{dt} = K_T\,\nabla^2 T, \tag{2. 18}$$

$$\frac{dS}{dt} = K_S\,\nabla^2 S, \tag{2. 19}$$

where K_T is the thermal diffusivity (conductivity divided by the product of density and heat capacity, all for seawater) and K_S is the salt diffusion coefficient. The values of these two coefficients are variable depending on the phenomena under study and play a key role at small-scale processes. Therefore, K_T and K_S must be tuned to fit our purposes.

Solving this set of equations any relevant process in the ocean could be represented. Its complexity is obvious, so we rely on numerical methods to solve it. For further details see Cushman-Roisin and Beckers (2011).

Numerical modelling: MITgcm

The Massachusetts Institute of Technology general circulation model (MITgcm, http://mitgcm.org) is a very versatile tool for modelling fluid dynamics problems, since it has been developed to resolve a wide-scale range of processes (Marshall et al., 1997a, 1997b). In the ocean, it permits simulating from local turbulent fluxes to global ocean circulation, under both realistic and idealized set-ups. It has been widely used in researches focused on submarine melting and fjord circulation modelling (Carroll et al., 2015; Cowton et al., 2015; Sciascia et al., 2013; Slater et al., 2015; Xu et al., 2012, 2013).

The MITgcm is a substantially evolved version of the finite-volume software initially developed by Marshall et al. (1997a, 1997b). It solves the *Boussinesq* form of the Navier–Stokes equation set on a generalized curvilinear grid. The finite-volume discretization is rendered horizontally variable on either a regular cell grid (Arakawa and Lamb, 1977) or on an irregular shaved-cell grid (Adcroft et al., 1997), and vertically fixed on z-levels, which makes the model very suitable for representation of complex geometries, typical of ocean basins. The most computational demanding part of the algorithm is that of the pressure correction to the velocity field, which ensures that the evolving velocity field remains non-divergent, while it is efficiently implemented in the algorithm. The kernel algorithm is firmly rooted in the incompressible Navier-Stokes equations, but can be used under hydrostatic, quasi-hydrostatic and non-hydrostatic assumptions, which leads into the chance to use the model for high-resolution phenomena simulations, which is the case for sudden subglacial discharges. Moreover, the *finite volume approach*, in which property fluxes are defined normal to the faces that define the volume elements, leads to a very natural and robust discrete analogue of divergence.

The MITgcm also includes a routine, developed by Xu et al. (2012), where the thermodynamic equilibrium at the ice-ocean interface (Fig. 2.2.1) is implemented as boundary conditions, and icefront melt rates can be estimated.

How to run the fjord model

There are several steps to properly run MITgcm simulations (see Fig. 2.2.4). To facilitate future work, we briefly list these steps below, but specific detailed information can be found in MITgcm documentation (http://mitgcm.org).

1. Configuration of the code.

a) Packages to be used, in our case: Geophysical fluid dynamics, Open Boundaries, External forcing, Icefront thermodynamics and Diagnostics.

b) Assumptions implied: non-hydrostatic, free sea surface.

c) Grid domain size (nX, nY, nZ); time of simulation (runTime).

d) Number of CPUs to run in parallel (N tiles).

e) Files to be read: grid cell size (dx, dy, dz), time resolution (dt), bathymetry (bathy), initial conditions (IC), boundary conditions (BC), glacier front and subglacial discharge (Q_{sg}).

2. Compilation of the code and executable file generation: mitgcmuv.exe.

3. Routine to create readable files for the executable-file compiled.

4. Running the model.

5. Routine to extract data results and visualize the simulations.

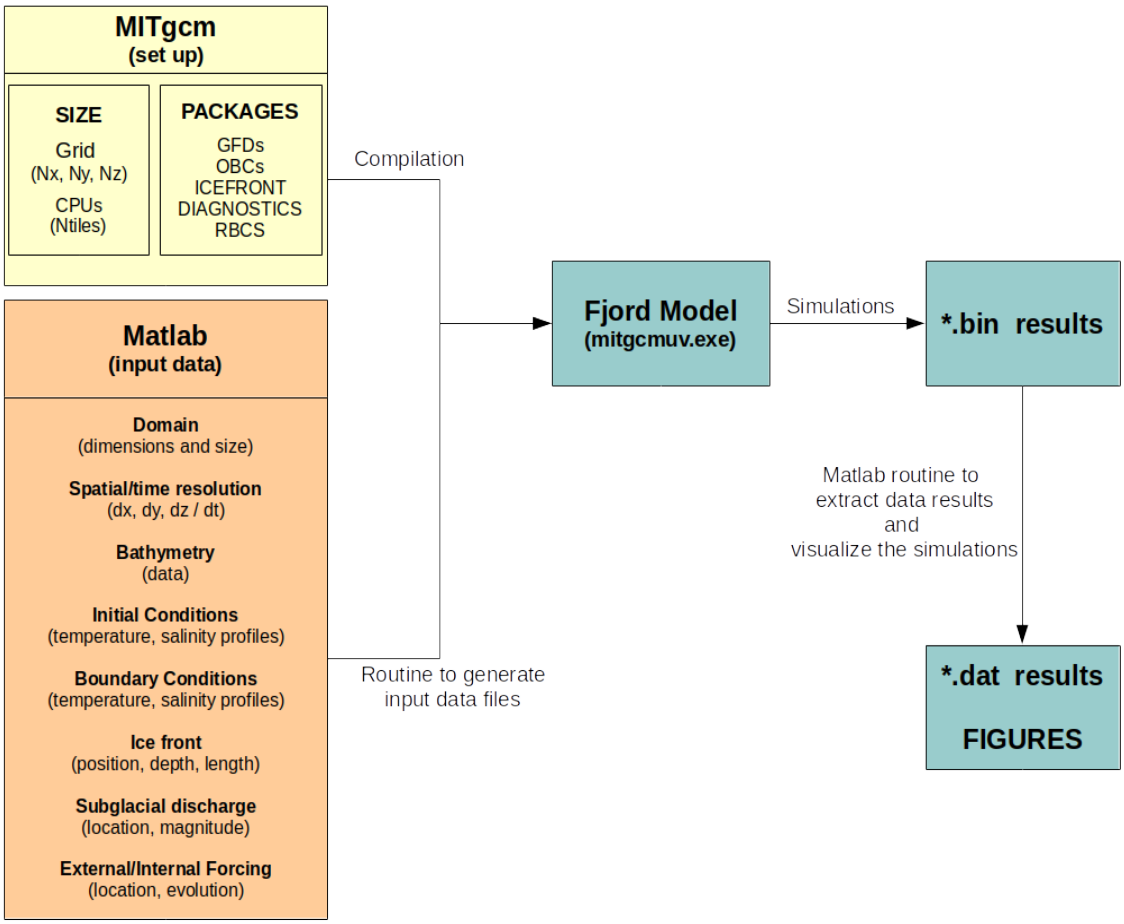

Figure 2.2.4 Schematics to run MITgcm simulations

Model set up and calibration

To adjust the model to our purposes, we first need to evaluate the sensitivity of the fjord model to free parameters and grid resolution (Fig. 2.2.5). We simulated a real fjord (Hansbukta, SW Svalbard, see physical settings in Section 2.2.2), where observations of fjord temperature and salinity were used as initial and boundary conditions. We tested the sensitivity of the modelled fjord temperature and salinity to viscous and diffusive coefficients and calibrated them to match the available observations of temperature and salinity. Then, subglacial discharge fluxes (Q_{sg}) were also tested and adjusted every two weeks from April to August of 2010. The sensitivity of submarine icefront melting and near-front temperature and vertical velocity to horizontal grid resolution were also evaluated.

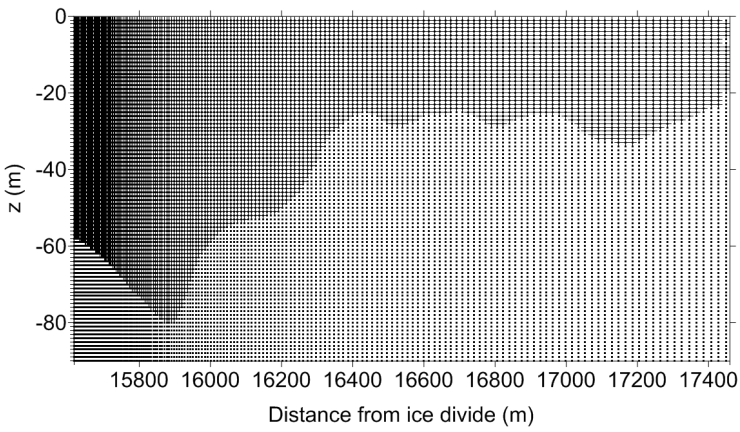

Figure 2.2.5 Fjord domain grid. The glacier front is located to the left and the fjord mouth to the right. Mean sea level is at z = 0 m and the fjord bottom (bathymetry) is represented by the interface between the darker and lighter parts (white part representing bedrock). Vertical grid resolution is constant (1 m) over the entire domain, while horizontal grid resolution is higher near the glacier front (1 m), with grid size linearly increasing to the fjord mouth (~40 m).

- Sensitivity of fjord properties to viscous ($\mathbf{A_{h,v}}$) and diffusive ($\mathbf{K_{h,v}}$) coefficients.

Since turbulent entrainment processes are parameterized by constant eddy diffusivity and viscosity (Eqns. 2.15 to 2.19), the correct orders of magnitude for these parameters are crucial to properly characterize the fjord model behaviour (Fig. 2.2.6). We run the fjord model during the first week of August 2010, varying both horizontal and vertical $A_{h,v}$ from 0.014 to 0.14 m^2 s^{-1}, and $K_{h,v}$ from 1.4 · 10^{-3} to 0.14 m^2 s^{-1}. The experiments showed that the horizontal and vertical salinity distribution in the fjord is strongly sensitive to both coefficients, $A_{h,v}$ and $K_{h,v}$, while this did not happen for temperature (Fig. 2.2.6). Combining our experiments with previous studies (Slater et al., 2015; Xu et al., 2013) we concluded that $A_{h,v}$= 0.014 m^2 s^{-1} and $K_{h,v}$= 0.0014 m^2 s^{-1} are the best-fit values, so they will be fixed for our purposes.

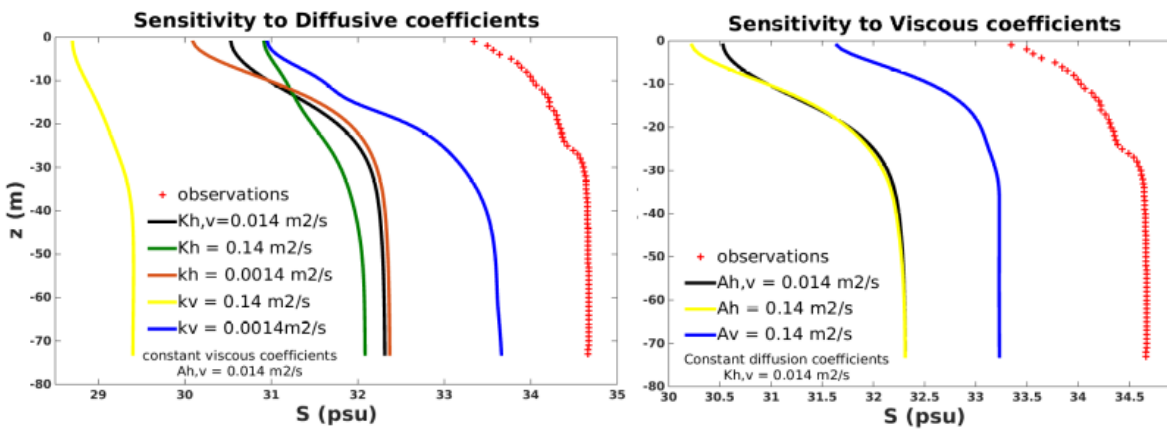

Figure 2.2.6 Modelled salinity profiles of Hansbukta fjord for different values of viscous ($A_{h,v}$) and diffusive ($K_{h,v}$) coefficients. Observed profiles are represented by red crosses.

- Sensitivity of fjord properties to subglacial discharge.

During the melting season, fjord surveys in the vicinity of the glacier front are difficult and risky due to the occurrence of iceberg calving. Thus, values of Q_{sg} are difficult to quantify due to the lack of observations near the front. For this reason, glacier mass balance models are commonly used to estimate surface melting (in response to atmospheric forcing), which are usually considered in the literature as immediate subglacial discharges. However, there is much uncertainty about the number and extent of the different catchments that collect this surface melting, the time that it takes the meltwater to reach the waters of the fjord, how much of the meltwater flows on the surface or subglacially, how is the network of discharge channels developed under the glacier body, or how many subglacial discharge channels, and of what size, inject the meltwater into the fjord. Due to all the above uncertainties, and given that we are using a 2D model (with spreading and diffusive limitations due to the lack of the third dimension), we decided to test the sensitivity of the vertical average of the modelled fjord temperature and salinity (excluding the first 5 m of the top layer, since we do not consider atmospheric forcing or melting of floating ice) to Q_{sg}. According to freshwater runoff estimates from Hansbreen in summer of 2010, and given that we have no data about size or number of discharging channels, we tested discharge velocities ranging from 0 to 0.2 m s^{-1} to assess a wide range of possibilities (Fig. 2.2.7). We then adjusted Q_{sg} values so they produced modelled temperature and salinity that best matched observations every two weeks, ensuring better submarine melt rates estimates. The resulting best-fit Q_{sg} fluxes (velocities implemented through a 1 m^2-grid cell) ranged from 10^{-3} in early April to $5{\cdot}10^{-2}$ m^3 s^{-1} in August, and they were used in our coupled-model studies (De Andrés et al., 2018 and De Andrés et al., 2021, respectively).

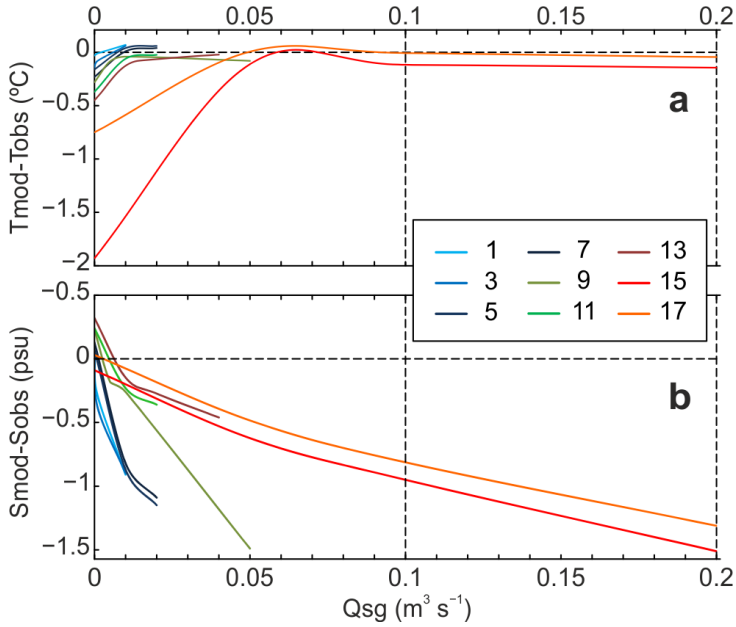

Figure 2.2.7 Sensitivity of the model to subglacial discharge fluxes in terms of a) temperature and b) salinity. Different colors are used for representing each simulated time period (weeks 1-17), see the legend.

- Sensitivity of the fjord model to grid resolution.

Sensitivity of submarine melt rates to spatial grid resolution was tested within a period of maximum melting, using Q_{sg} of 0.1 m³ s⁻¹ and August-2010 fjord properties. Horizontal size of the grid cells embedded into the high-resolution zone of the domain were varied (while maintaining the same order of magnitude) from 0.9 to 4 m, so no variations in viscous or diffusive coefficients were needed. Submarine melt rates were calculated and compared, and the results are shown in Fig. 2.2.8. The analysis of sensitivity to horizontal resolution was made in terms of vertical velocity (tangential to the front face) and temperature, which are the dominant controls on determining submarine melt rates. The temporal averages of both variables were calculated over the simulation period, and the maximum values of both variables were identified along the water column, in the cells immediately adjacent to the glacier front. The same calculations were made for the submarine melt rates estimated by the model.

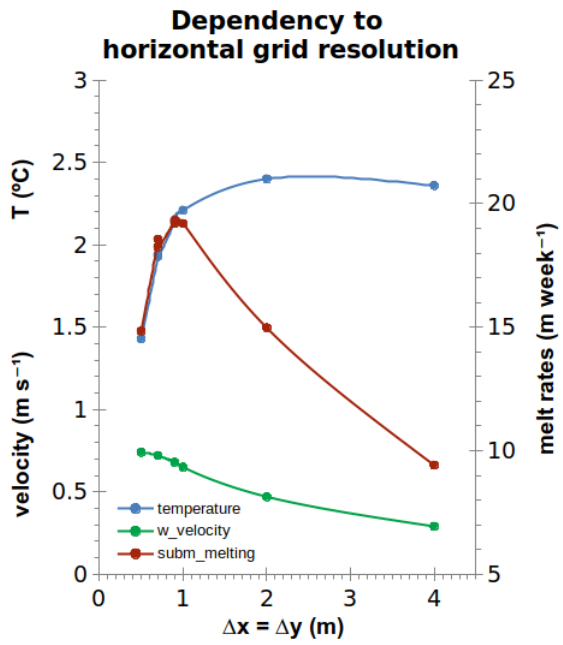

Figure 2.2.8 Sensitivity of the modelled variables to spatial resolution. Temperature (T) in blue, vertical velocity (w) in green and submarine melt rates (SMR) in red. Kinematic viscosity and diffusive coefficients set to 0.014 and 0.0014 m^2 s^{-1}, respectively, and time step fixed to 0.5 s.

The minimum cell size that allowed the stability of the model without changing the size of the time step was 0.9 m. The maximum cell size that allows us to use the same coefficients (viscosity and diffusion) without involving a change of their order of magnitude, is 4 m. From Fig. 2.2.8, it is inferred that the temperature in the cells contiguous to the front varies slightly (<9% across the range of cell sizes), which indicates that the plume-environment mixing processes are well resolved. However, the maximum speeds reached in these cells vary enormously (~ 50%) with decreasing grid-cell resolution. This suggests that the kinematic viscosity coefficients used in our model are valid only for cell sizes of 1 m or less, considering that the time step should be adjusted for cell sizes smaller than 0.9 m. For cell sizes greater than 1 m, the value of the viscous coefficients should be adjusted, in order to account for the (probably turbulent) unresolved processes and to reach the expected speeds. This sensitivity of velocity to spatial resolution also translates into sensitivity in terms of submarine melting estimates. Thus, the maximum melt rates take place for cell sizes of 0.9 and 1 m, with almost zero variation between both (~ 0.1%). Therefore, we can state that our model is adequately resolving the velocity and temperature fields in the vicinity of the front for 1-m cell resolution, assuring the optimum values of submarine melt rates.

COMPONENT 3: THE SUBMARINE MELT MODEL

The thermodynamic melt rate ($\dot{m}$) parameterization of the ice-ocean boundary is based on the set of three equations developed by Holland and Jenkins (1999), where subscripts *b*, and *i* indicate boundary and ice, respectively:

$$T_b = \lambda_1 S_b + \lambda_2 + \lambda_3 p_b, \tag{2. 20}$$

$$C_{pw}\rho\gamma_T(T - T_b) = -\dot{m}\left[L_f + C_{pi}(T_i - T_b)\right], \tag{2. 21}$$

$$\rho\gamma_S(S - S_b) = -\dot{m}(S_b - S_i). \tag{2. 22}$$

The first equation (2.20) represents a linearization of the liquidus relationship (i.e. the freezing temperature of seawater at a given depth), where T_b , p_b , and S_b are the temperature, hydrostatic pressure, and salinity at the ice-ocean boundary, respectively. For seawater, $\lambda_1 = -5.73 \cdot 10^{-2}$ ºC is the freezing point slope; $\lambda_2 = 8.32 \cdot 10^{-2}$ ºC is the freezing point offset; and $\lambda_3 = 7.61 \cdot 10^{-4}$ ºC m^{-1} is the depth-dependent freezing point slope. Conservation of heat and salt in the ice-ocean thermodynamic equilibrium are represented by equations 2.21 and 2.22, where the specific heat capacity for seawater (C_{pw}) and ice (C_{pi}) take the values of 3974 and 2009 J kg^{-1}K^{-1}, respectively. The velocity-dependent turbulent transfer coefficients of heat and salt, $\gamma_{T,S}$, are also considered proportional to the plume vertical velocity:

$$\gamma_{T,S} = C_d^{1/2}\Gamma_{T,S}U, \tag{2. 23}$$

where $C_d^{1/2}$ and $\Gamma_{T,S}$ are the drag and turbulent-transfer coefficients, respectively. The thermal and haline Stanton numbers are defined by $C_d^{1/2}\Gamma_{T,S}$, for which we take the values proposed by Jenkins et al. (2010) (see also Table 2.2.1 at the end of this section).

COMPONENT 4: THE LINE PLUME MODEL (De Andrés et al., 2020, 2021)

The parameterization of the buoyant plume formed by discharges of subglacial meltwater is described here. The buoyant plume theory is a common tool for gaining insight into plume dynamics and the dominant controls on their variability (Carroll et al., 2015, 2016; Cowton et al., 2016; Jenkins, 2011). The limited information we have on plume geometry suggests that the truncated line plume model (Jenkins, 2011) (Fig. 2.2.9) is the most appropriate one for plumes driven by subglacial discharge at tidewater glaciers (Fried et al., 2015; Jackson et al., 2017).

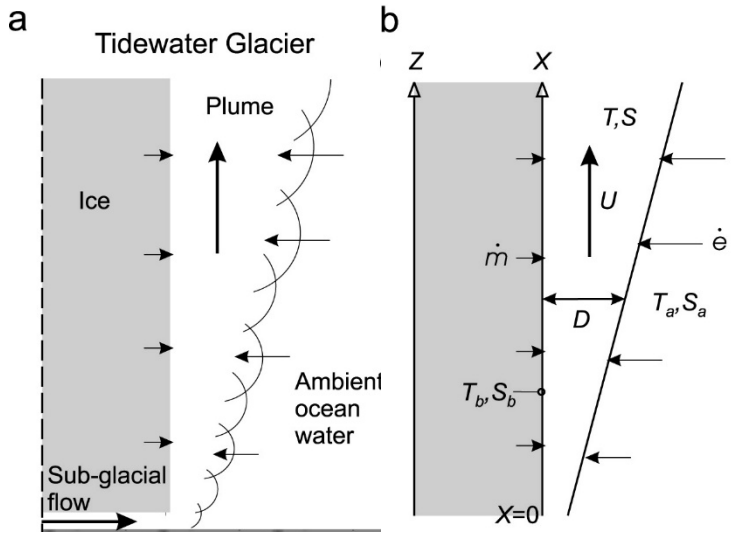

Figure 2.2.9 Schematics of a) the buoyant plume formed from freshwater subglacial discharges in tidewater glaciers, and b) the 1D-line plume model representing the buoyant plume phenomenon (from Jenkins, 2011).

Mathematical formulation of buoyant line-plumes

The model is steady in time and homogeneous over the plume cross-section ("top hat"), leaving the along-flow direction (z in our case, assuming vertical ice face) as the only independent variable. The evolution of the plume properties, thickness (D), vertical velocity (U) and density (ρ) along the vertical tidewater face, is described by three ordinary differential equations that express the conservation of fluxes of mass, momentum and buoyancy:

$$\frac{d}{dz}(DU) = \dot{e} + \dot{m}\,, \tag{2. 24}$$

$$\frac{d}{dz}(DU^2) = Dg' - C_d u^2\,, \tag{2. 25}$$

$$\frac{d}{dz}(DU\rho) = \dot{e}\rho_a + \dot{m}\rho_b - \gamma(\rho - \rho_b)\,, \tag{2. 26}$$

where subscripts a and b indicate ambient and boundary (at the ice-ocean), respectively.

The reduced gravity is defined as

$$g' = g\frac{(\rho_a - \rho)}{\rho_0}, \tag{2. 27}$$

and the entrainment rate is considered as a linear function of the plume velocity, i.e.

$$\dot{e} = \alpha\, U\,, \tag{2. 28}$$

where α is the entrainment coefficient.

Since ρ is calculated from observations of temperature and salinity, Eq. 2.26 is split in two equations which conserve the fluxes of heat and salt in the plume, such that:

$$\frac{d}{dz}(DUT) = \dot{e}T_a + \dot{m}T_b - \gamma_T(T - T_b)\,, \tag{2. 29}$$

$$\frac{d}{dz}(DUS) = \dot{e}S_a + \dot{m}S_b - \gamma_S(S - S_b)\,. \tag{2. 30}$$

Turbulent transfer coefficients of heat and salt, $\gamma_{T,S}$, where previously defined in Eq. 2.23 and are both dependent on the plume velocity.

The plume model is closed using the thermodynamic equation of state (TEOS-10, McDougall and Barker, 2011) to calculate the plume and ambient densities (ρ and ρ_a, respectively) and the melt rate, $\dot{m}$ (also denoted R_m), calculated by virtue of Eqns. 2.20-2.23, which state the heat and salt balance at the ice-ocean interface as well as the requirement that the interface temperature is at the local freezing point (previously described in Section 2.2.4).

Numerical modelling and calibration

The MATLAB software was selected to build up our routine to solve the above-described line-plume model equations. The model is initialized by prescribing the ambient conditions, $T_a(z)$ and $S_a(z)$, a given width of the subglacial channel (W) and the velocity at which the freshwater is discharged through the subglacial channel ($U_{sg} = Q_{sg}/A_{channel}$). Sensitivity analysis of plume properties to $S_a(z)$ and Q_{sg} were performed to evaluate the plume model behaviour and to calibrate α.

- Model sensitivity to the entrainment coefficient ($\boldsymbol{\alpha}$):

We run our plume model considering a 150-m deep fjord, a fixed W of 100 m and a constant Q_{sg} of 120 m^3 s^{-1}. To simulate the ambient fjord waters, we assumed a linearly stratified water column due to salinity gradient, such that $S_a(z = 0) = 26$ g kg^{-1} and $S_a(z = -150) = 34$ g kg^{-1}, while maintaining constant temperature, $T_a(z) = 1$ ºC. Based on specialized plume-model literature (Carazzo et al., 2006; Kaminski et al., 2005) and fjord-applied studies (Mankoff et al., 2016; Slater et al., 2016; Stevens et al., 2016) we run our model for values of α ranging from 0.08 to 0.12. According to Eq. 2.28, higher values of α lead into larger entrainment rates of ambient waters into the plume, causing heavier, wider and slower plumes, which also translate into smaller melt rates (R_m) (Fig. 2.2.10). For our coupled model, we will use $\alpha = 0.1$, since it is an intermediate value and has been successfully used in multiple line plume model studies (Jackson et al., 2017; Slater et al., 2016).

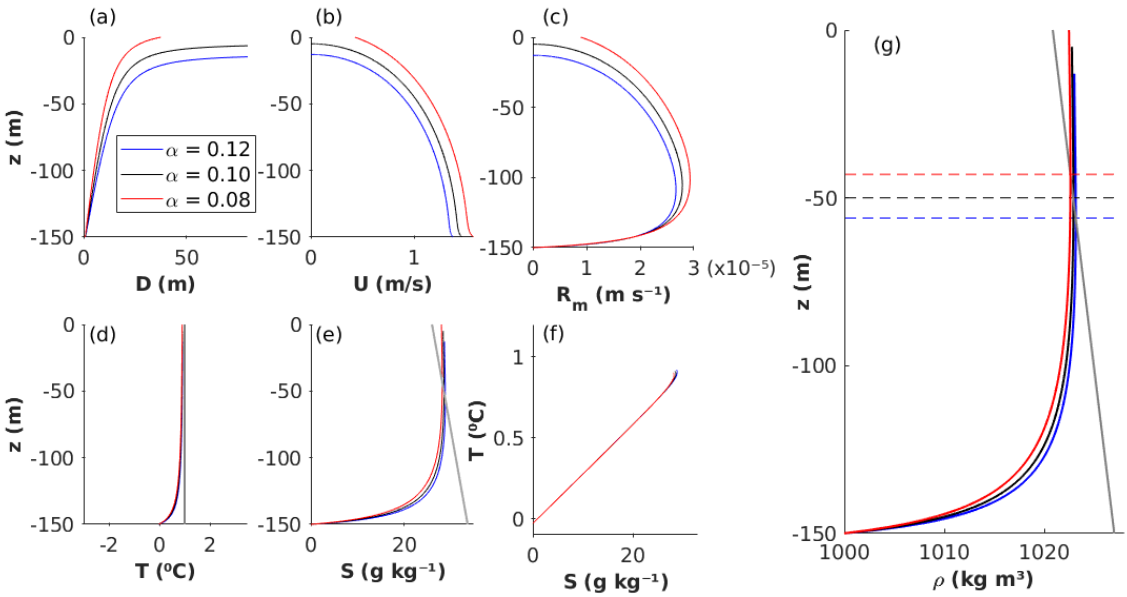

Figure 2.2.10 Modelled plume-vertical profiles of a) thickness, b) velocity, c) melt rate, d) temperature, e) salinity, f) T-S diagram and g) density, resulting from different values of α (0.12 in blue, 0.10 in black and 0.08 in red). Ambient profiles are shown in grey lines.

- Model sensitivity to ambient salinity ($\boldsymbol{S_a(z)}$) and subglacial discharge ($\boldsymbol{Q_{sg}}$):

In this test, we run our plume model considering also a 150-m deep fjord and a fixed W of 100 m. Using constant $\alpha = 0.1$, Q_{sg} was varied here from 60 to 180 m^3 s^{-1}. We tested the model performance under two configurations for the ambient fjord waters. The first one equals those of the previous experiment: we assumed a linearly stratified water column due to salinity gradient, such that $S_a(z = 0) = 26$ g kg^{-1} and $S_a(z = -150) = 34$ g kg^{-1}. The second configuration becomes simpler by assuming a constant salinity profile, $S_a(z) = 34$ g kg^{-1}. Both configurations keep a constant temperature profile, $T_a(z) = 1$ ºC. Regarding the impact of Q_{sg}, we observe that, for both ambient configurations, higher fluxes produce higher plume velocities (Fig. 2.2.11b), which translates into higher melt rates (Fig. 2.2.11c) than those obtained from lower Q_{sg} fluxes. Moreover, the higher the Q_{sg}, the lighter the plume, which reaches its neutral buoyancy (plume density equals ambient density, just for the stratified configuration) at a depth higher up than those heavier plumes resulting from lower discharge fluxes (see dashed horizontal lines in Fig. 2.2.11g). The effects of ambient salinity on modelled plume properties are shown in Fig. 2.2.11 (red lines are for the linearly stratified ambient waters and blue lines for uniform ambient profiles). We see how stratification exerts a dampening effect on plume velocity, resulting on slower, thicker and lighter plumes. Stratification also reduces the submarine melt rates along the glacier front (Fig. 2.2.11c) and promotes plume suppression of the neutral buoyancy depth (Fig. 2.2.11g). To diminish the errors caused by these two variables in our coupled model, Q_{sg} and $S_a(z)$ will be inferred and constrained, respectively, from observations.

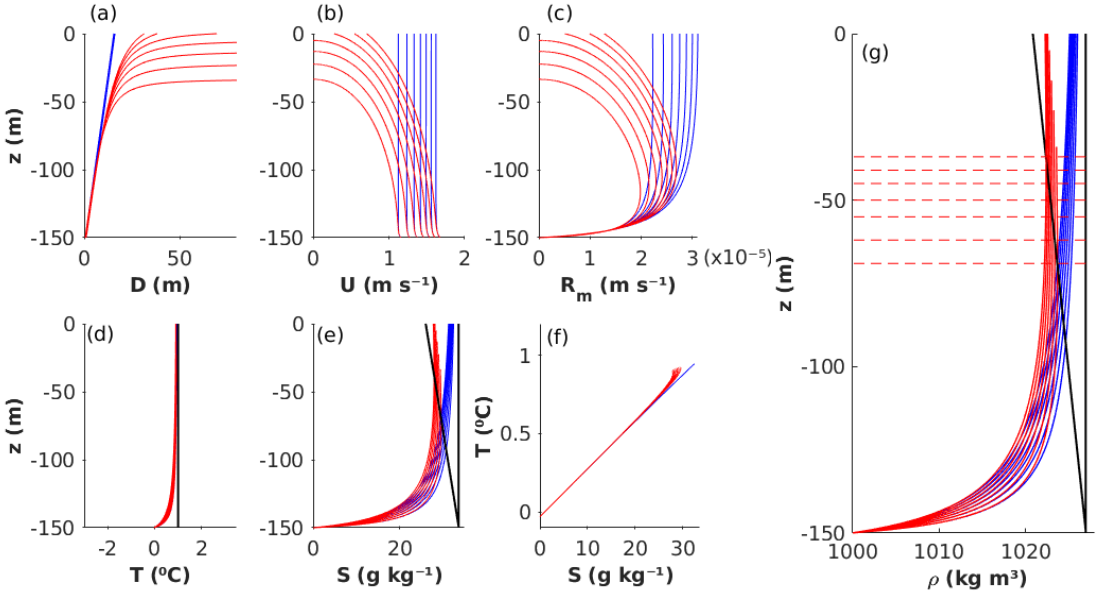

Figure 2.2.11 Plume model results from considering Q_{sg} from 60 to 180 m^3 s^{-1} under two different ambient profiles. Red lines are results from linearly stratified fjord waters and blue lines from vertically homogeneous fjord properties. The modelled plume properties are a) thickness, b) velocity, c) melt rate, d) temperature, e) salinity, f) T-S diagram and g) density. Black lines correspond to the ambient profiles.

COUPLING THE ICE-OCEAN MODEL COMPONENTS

We begin by describing the glacier-fjord coupled model. Both the glacier and the fjord models are asynchronously called by an offline master script, whose code we wrote in GNU bash (Unix shell). The latest version developed and run in this project was the *"script_for_coupling_model_v6.sh "*. As sketched at the beginning of this Section 2.2.1, the coupling between our glacier and fjord models is accomplished through two main mechanisms (see schematics of Fig. 2.2.12): 1) Depth-dependent submarine melt rates, $\dot{m}(z)$, are daily estimated and weekly integrated, $SMR(z)$, by the fjord model. These $SMR(z)$ are used to modify the shape of the submerged part of the glacier front (Fig. 2.2.12). The resulting changes in the front shape define a new glacier model domain, which is remeshed by the glacier model and might imply changes in the glacier stress regime near the front (Todd and Christoffersen, 2014). 2) Front position changes resulting from the glacier dynamics model modify the fjord domain length and the submerged part of the front. The submerged ice front (left fjord boundary) is assumed to remain vertical at any time (even in the absence of iceberg calving), since changes in ice-front shape does not have a significant effect on submarine melt rates (Slater et al., 2017). Velocity fields in the fjord are linked to grid cell position rather than actual locations. Although this implies a potential shift of the fjord velocity field, we ensure coherent motion near the glacier front at each simulated week. Following similar studies (Seroussi et al., 2017), glacier and fjord models are run with different spatial and time resolutions to ensure appropriate simulation of the relevant processes involved in each model. They run asynchronously and automatically, exchanging information every modelled week. The choice of this frequency of intercommunication between both models is supported by two main arguments: 1) there is no significant variation in submarine melting within a single week of simulation, and 2) the glacier-model time-step is one week.

Note that our fjord model is unable to reproduce any variation of potential forcing with a time scale shorter than a week, such as short-term variations in subglacial discharge intensities (peaks in surface melting due e.g., to heavy rain events or surface temperature peaks) or sudden intrusions of Atlantic-water masses through the fjord mouth. Although the submarine melt rates might vary significantly because of these processes, the available observations are too sparse to account for them.

The latest version of the glacier-plume coupled model developed and run in this project was the "*script_for_coupling_plume_model_v6.sh* ". As described above for the glacier-fjord model, the coupling between our glacier and plume models is also accomplished through the same two main mechanisms (see schematics of Fig. 2.2.12): 1) Depth-dependent submarine melt rates are estimated weekly by the plume model and used to modify the morphology of the submarine glacier front. The glacier model is run with a new domain, which is accordingly remeshed to fit the new front geometry. 2) Front position changes resulting from the glacier dynamics model modify vertical plume domain (the submerged part of the front), which is assumed to be vertical at any time (Slater et al., 2017).

In order to facilitate the information for the reader, all parameters and some model variables used in our coupled model have been summarized in Table 2.2.1.

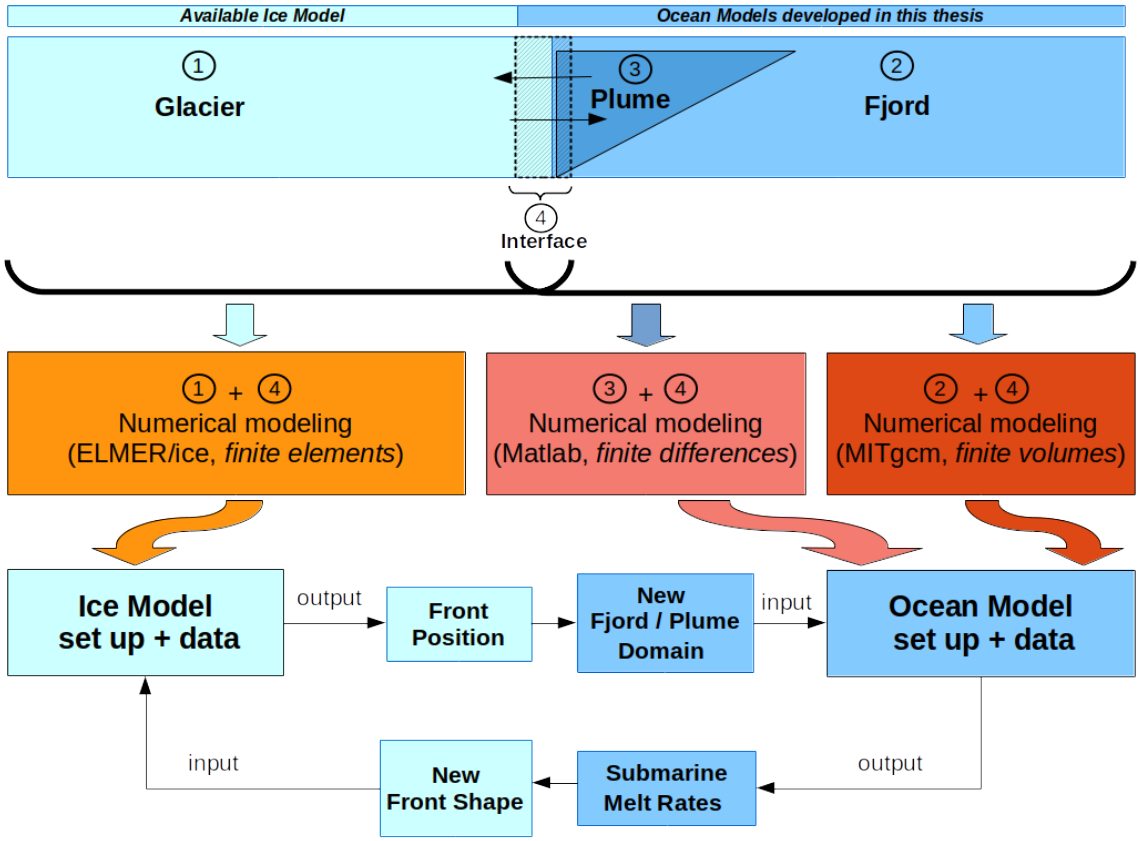

Figure 2.2.12 Flow diagram of modelling and coupling among the different system components.

Table 2.2.1 Model variables and parameters used within Section 2.2.1, grouped in terms of the different components of the coupled model.

Parameter/variable	Description	Value and units/ Equation/s (units)
g	Gravity acceleration	9.8 m s^{-2}
Glacier component		
ρ_i	Ice density	917 kg m^{-3}
f_s	Shape factor	Eq. 2.3
w_h	Half width at the glacier surface	From observations (m)
η	Effective viscosity	Eq. 2.5
n	Power for polythermal glaciers	3
A_i	Glen's softness parameter	0.1 bar^{-3} a^{-1}
E	Enhancement factor	1 to 4.6
D	Scalar local damage	0 to 0.4
b_n	Surface mass balance	From observations (m week^{-1})
C	Bottom-friction coefficient	From inversion, Eq. 2.9
d	Crevasse depth	From tuning (m)
Fjord component		
ρ	Seawater density	Eq. 2.11
ρ_0	Seawater reference density	1028 kg m^{-3}
T_0	Reference ocean temperature	10 ºC
S_0	Reference ocean salinity	35 psu or g kg^{-1}
α_T	Thermal expansion coefficient	$1.7 \cdot 10^{-4}$K^{-1}
β_S	Saline contraction coefficient	$7.6 \cdot 10^{-4}$
f_*	Reciprocal Coriolis parameter	$\sim 10^{-4}$ s^{-1}
$A_{h,v}$	Viscous kinematic coefficient	0.014 to 0.14 m^{2}s^{-1}
H	Water depth	From bathymetry obs. (m)
K_T	Thermal-conductivity coefficient	0.0014 to 0.14 m^{2}s^{-1}
K_S	Salt diffusive coefficient	0.0014 to 0.14 m^{2}s^{-1}
Q_{sg}	Subglacial discharge flux	From observations (m^3 s^{-1})
SMR	Weekly submarine melt rates	From $\dot{m}$, Eqns. 2.20-2.22 (m week^{-1})
Interface component		
λ_1	Freezing point slope for seawater	$-5.73 \cdot 10^{-2}$ ºC
λ_2	Freezing point offset	$8.32 \cdot 10^{-2}$ ºC
λ_3	Depth-dependent freezing point	$7.61 \cdot 10^{-4}$ ºC m^{-1}
C_{pw}	Specific heat capacity for seawater	3974 J kg^{-1}K^{-1}
C_{pi}	Specific heat capacity for ice	2009 J kg^{-1}K^{-1}
$C_d^{1/2}\Gamma_T$	Thermal Stanton number	$1.1 \cdot 10^{-3}$
$C_d^{1/2}\Gamma_S$	Haline Stanton number	$3.1 \cdot 10^{-5}$
$\dot{m}$	Melt rates	From Eqns. 2.20-2.22 (m s^{-1})
Plume component		
C_d	Drag coefficient	$2.5 \cdot 10^{-3}$
$\dot{e}$	Entrainment rate	From Eq. 2.28
α	Entrainment coefficient	0.08 to 0.12

2.2.2. Partitioning into calving and submarine melting using the coupled models. A case study for Hansbreen-Hansbukta glacier-fjord system

PHYSICAL SETTINGS & DATA

Hansbreen Glacier−Hansbukta Fjord system is a branch of the Hornsund fjord, in South−west Spitsbergen, Svalbard, at ~ 77 °N (Fig. 2.2.13a). Hansbreen is a tidewater glacier about 16 km long and 2.5 km wide. It has a 1.5 km−wide calving front, with a vertical face that is ~ 100 m−thick at the central flowline, of which 50−60 m are submerged. Surface velocity increases towards the terminus, reaching values up to ~ 7 m week^{-1} (Fig. 2.2.13b). Iceberg calving usually starts in May and ends in October, showing a mean annual calving rate of ca. 250 m a^{-1} between 1989 and 2000 (Blaszczyk et al., 2009). Hansbukta is a ~ 2 km−long and shallow fjord (< 80 m in depth), with water depth close to the central part of the glacier front of around 55−57 m.

Observational input data to the glacier model include surface velocities, front positions, ice−mélange coverage, surface elevation, bedrock topography and surface mass balance. Ice surface velocities (Fig. 1b) were measured daily, from May 2005 to April 2011, at stakes located close to the flowline (Puczko, 2012) and from terrestrial laser scanner for the velocities at the glacier terminus (data provided by Jacek Jania [University of Silesia] from surveying and data processing by Jacek Krawiec [Laser 3D], Artur Adamek [Warsaw University of Technology] and Jacek Jania). Front position data and ice−mélange coverage from time−lapse camera images taken every three hours (Fig. 2.2.13c) were processed and averaged over weekly intervals between December 2009 and September 2011 (Otero et al., 2017). Surface mass balance (SMB) was obtained from European Arctic Reanalysis (EAR) data, with 2 km horizontal resolution and hourly temporal resolution, constrained by automatic weather stations and stake observations (Finkelnburg, 2013). Mean SMB and surface meltwater (SMW) at each flowline point was calculated by applying bilinear interpolation to the available 2−km resolution hourly accumulation and ablation data (Fig. 2.2.13c). The surface elevation came from the SPIRIT Digital Elevation Model (DEM) for gentle slopes, with a 30 m root−mean−square (RMS) absolute horizontal precision and 40 m resolution. Bedrock topography was inferred from ground−penetrating radar (GPR) data (Grabiec et al., 2012; Navarro et al., 2014).

Available oceanographic data overlap glaciological data only from April to August of 2010, limiting our modelling period to ~20 weeks. Oceanographic data consists of conductivity−Temperature−Depth (CTD) profiles in Hansbukta (Figs. 2.2.13d, e). All the data were vertically averaged every 1 dbar (1 kPa). Data gaps (CTDs for missing weeks) were linearly interpolated, maintaining the vertical structure of the water column (i.e., the interpolation was applied to each vertical level; Fig. 2.2.13d, e). Temperature (salinity) in Hansbukta experience strong seasonal variability, ranging from −1.8 to 3 °C (34.6 to 31.8 g kg^{-1}), from April to August, respectively.

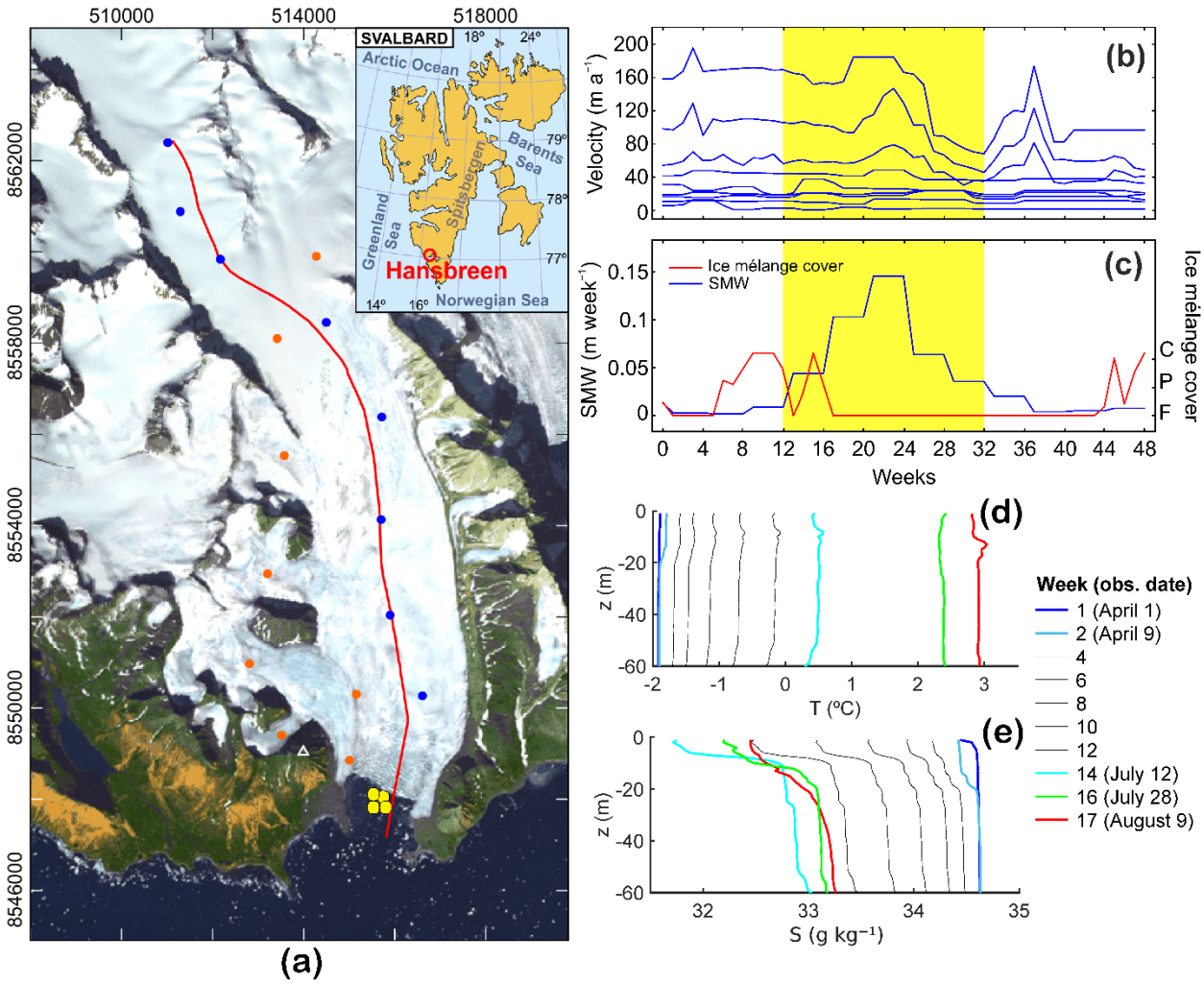

Figure 2.2.13 a) Hansbreen−Hansbukta system, Svalbard (inset), displayed on an ASTER image in UTM coordinates (m) for zone 33X. The white triangle represents the position of a time−lapse camera used to measure front position. The modelled flowline is defined by the red line (extended into Hansbukta) and blue dots indicate the locations of the stakes for velocity measurements (orange dots are not used in our analysis). Yellow circles in Hansbukta indicate the location of the CTD stations (~ 300 m from front) used to provide ambient fjord−water properties; time evolution of b) ice surface velocities, increasing towards the terminus and measured at the blue stakes in a); c) surface meltwater estimates (SMW, blue line) and ice mélange cover (red line; F: free, P: partial, C: complete); and d) temperature and e) salinity profiles in Hansbukta (measured at yellow CTD stations in a), from April 1 to August 9, 2010, coincident with the yellow region in b) and c). Coloured lines represent observations. Grey lines are interpolations, showing a continuous warming (freshening) in temperature (salinity) with time.

EVALUATION OF THE PERFORMANCE OF THE COUPLED MODELS

We here analyse the differences between the coupled glacier−fjord and glacier−plume models and their performance on predicting the observed glacier front positions, so we can evaluate the goodness of each coupled model. Note that both models were run under weekly forcing. Therefore, given the steady-state nature of the plume model, there is just a weekly estimation of submarine melt rates. The transient fjord model, however, allows to estimate weekly submarine melt rates based on daily calculations. With our experimental design, our results do not provide information on the differences in submarine melting under equal conditions (which has been already addressed, e.g. Carroll et al., 2015), but on what each model is capable of representing under equal forcing conditions, and its effects in terms of submarine melting, calving rates and front position changes.

Submarine melting

A common characteristic for both models is that submarine melt rates (SMR) increase as summer progresses (Fig. 2.2.14), becoming maximum in week 17 (early August). We can interpret that part of this increase in submarine melting is due to warmer fjord waters and the increase in Q_{sg} as summer progresses (Fig. 2.2.13b, d). The SMR produced until week 7 is similar in both models, < 1 m week^{-1}, and it is consistent with the low Q_{sg}/W (≤ 0.002 m^3 s^{-1}) and with the ambient temperature (< −1 °C) during these weeks (see Fig. 2.2.13d). An important aspect is that maximum SMR takes place at the sea surface (Fig. 4a) in the glacier-plume model. Having in mind that temperature profiles in Hansbukta are vertically quasi−homogeneous (Fig. 2.2.13d), the fact that maximum SMR occurs in the vicinity of sea level is the result of plume velocities and temperatures being highest at that level (e.g., around 0.53 m s^{-1} and 2.8 °C, respectively, in week 16). This aspect differs from the results obtained with the fjord model, in which the melting profile indicates that the maximum SMR occurs at intermediate depths, at around 30 m (Fig. 2.2.14), where velocities and temperatures reach, for example, 0.55 m s^{-1} and 2.6 °C, respectively, in week 17.

In the case of the glacier-fjord model, the maximum SMR between weeks 1 and 11 is lower (there is even refreezing), ranging from ~ 0.01 m week^{-1} in April to ~ 2 m week^{-1} at the end of June. That is, the relative differences in maximum SMR between both models are larger in the first week, by approximately 90%, becoming smaller as they approach week 11, when the relative difference between maximum SMR is reduced to 33%.

From week 11 the glacier-plume model (-fjord model) shows maximum SMR of ~ 4 (2.5) m week^{-1}, obtained in week 12 –early July– and ~ 16 (16) m week^{-1} during weeks 17 and 18 –middle August. The relative differences between the maximum SMR obtained with both models is reduced as the summer progresses up to week 17 (SMR differences are minimum), then starting to grow again, but with maximum SMR higher for the fjord model.

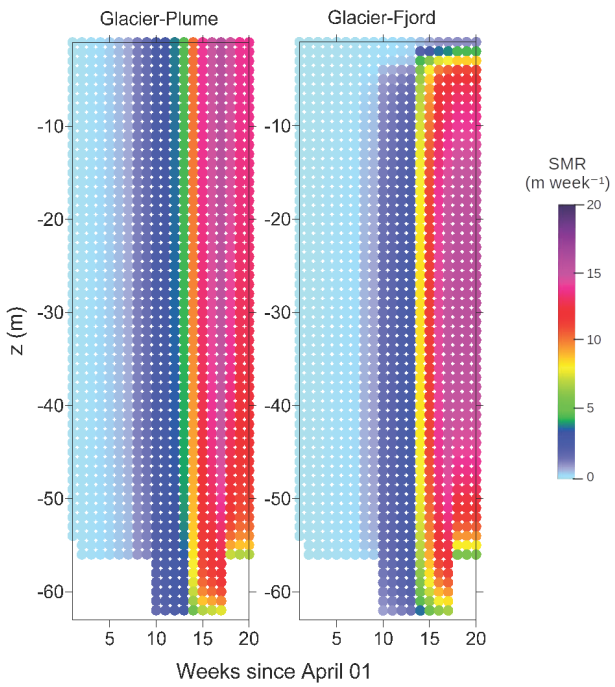

Figure 2.2.14 Time−evolution of weekly submarine melt rates (SMR) estimated with (a) the glacier−plume and (b) the glacier−fjord models. The submerged part of the ice front (all the coloured parts of the panels) increases with time, as a consequence of Hansbreen advance towards Hansbukta basin.

Front position

In the absence of water in crevasses, both the glacier−plume and the glacier−fjord models exhibit a similar pattern of continuous advance of the glacier front and no calving events when submarine melting is not taken into account (Scenario 0 in Fig. 2.2.15a, b). Both models show discontinuous progress under scenarios 1 and 2 of melting (realistic and enhanced scenarios, respectively), indicating that stronger subglacial discharge might lead to more calving. However, there is no difference in cumulative calving between scenarios 1 and 2 in the glacier−plume model, while a difference is observed in the glacier−fjord model (Fig. 2.2.15c). In scenarios 1 and 2, the first calving event occurs one week earlier (week 14) in the plume model compared with the fjord model (week 15). The total frontal ablation over the summer due to calving, under Scenario 1 (Scenario 2), amounts to ~ 32 (30) m in the plume model, while for the fjord model it is of ~ 17 (32) m (Fig. 2.2.15c). This might indicate that higher submarine melting in the fjord model amplifies the instability of the glacier front, promoting more calving. Overall, the three melting scenarios tested in our experiment predict glacier front positions more advanced than those observed, which means that submarine melting alone is not able to reproduce the observed front position.

Keeping fixed the more realistic melting scenario of subglacial discharge (Scenario 1, see sensitivity tests in Section 2.2.2, COMPONENT 2: THE FJORD CIRCULATION MODEL), we analyse the effect that different values of crevasse water depth Dw (0, 2 and 3 m, kept constant throughout the simulation period) cause on the front position for the glacier−plume (Fig. 2.2.15d) and glacier−fjord (Fig. 2.2.15e) coupled models. The most evident feature in both cases is the positive relationship between Dw and calving. With $Dw \neq 0$, the first calving event occurs between weeks 10−11 in both models, but for Dw = 2 m (Dw = 3 m), the plume model accumulates a total of ~ 70 (82) m of calving, higher than the 62 (73) m obtained with the fjord model (Fig. 2.2.15f). With identical configurations, both models predict very similar front positions. In both models, the best−fit corresponds to Dw = 2 m, with a root−mean−squared error (RMSE) with respect to observations of ~ 12 m.

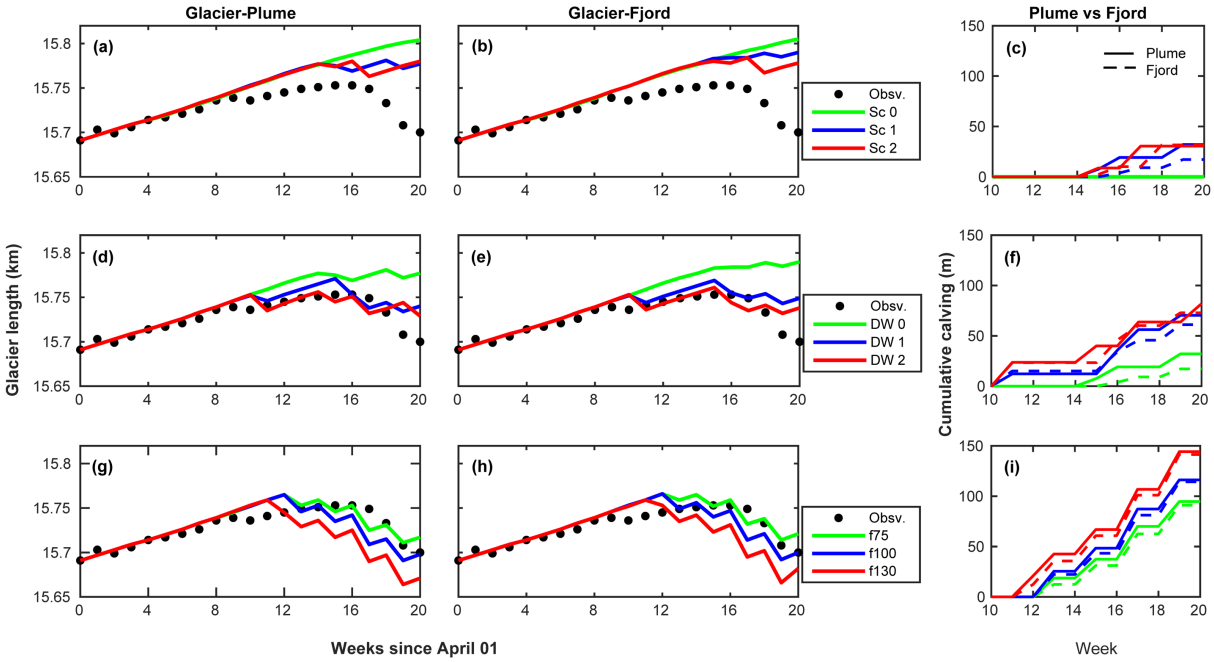

Figure 2.2.15 Time−evolution of Hansbreen front position and cumulative calving (right panels) resulting from the glacier−fjord (middle panels) and glacier−plume (left panels) models: (a), (b) and (c), the model run with no influence of crevasse water pressure (Dw = 0 m) and assuming three different scenarios of submarine melting; (d), (e) and (f), realistic submarine melt scenario (Sc 1) and three different values of Dw (0, 2, 3 m); (g), (h) and (i) the model also runs with Sc 1 of melting, but Dw is now a function of surface melting (with f−ratios of 75, 100 and 130. Observed front positions are represented with black dots.

In a second experiment, we set Dw as proportional to the surface melting throughout the summer, i.e., $Dw \propto f \cdot SMW$ (see Fig. 2.2.13c), and analyse the sensitivity of the front position to parameter f under melting Scenario 1. In Figs. 2.2.15g and 2.2.15h, we present the front positions of Hansbreen obtained with the glacier−plume and the glacier−fjord models, respectively, for $f = 75, 100, 130$. As in the previous experiment, a positive relationship between Dw and calving rates is observed (Fig. 2.2.15i), though in this case as a function of parameter f. In the glacier−plume model, the first significant calving event occurs at week 11 for $f = 100$ and 130, and at week 12 for $f = 75$. These first calving events coincide with those of the glacier−fjord model, except for $f = 100$, whose first event takes place on week 12. However, none of the two models is able to capture the first observed calving event in week 10, as it was predicted when fixing $Dw = 2, 3$. The cumulative calving in the glacier−plume (glacier−fjord) model over the entire simulated period is 94 (91) m for $f = 75$, 116 (114) m for $f = 100$ and 144 (141) m for $f = 130$ (Fig. 2.2.15i). These results indicate that the submarine melting generated by the plume model has a similar effect on calving than that resulting from the fjord circulation model. The best fit configuration in both coupled models is that of Scenario 1 of melting and $f = 75$, for which the RMSE with respect to the observed front position is of ~ 10 m in both cases. In fact, the squared errors of the two models (under the best−fit configuration) calculated every week show similar deviations with respect to observations (Fig. 2.2.16). Overall, both best−fit model predictions overestimate the glacier front position (more advanced than observed), although larger deviations concentrate within weeks 10−12, with longer observed glacier lengths (Fig. 2.2.16), corresponding to the middle−end of June 2010. Such deviations coincide with the first and isolated retreat event observed, which is not reproduced at all by any model or scenario. In fact, the first simulated retreat actually occurs from week 12 to 13 for both models under the best−fit configuration. In the glacier−plume model, however, the largest deviation from observations is of 25 m and takes place on week 17 (see Fig. 2.2.15), when the glacier front starts an uninterrupted retreat. This differs from the glacier−fjord model, where the maximum deviation, of 21 m, occurs at the end of the simulation period (week 20), when the glacier has already retreated close to its initial position.

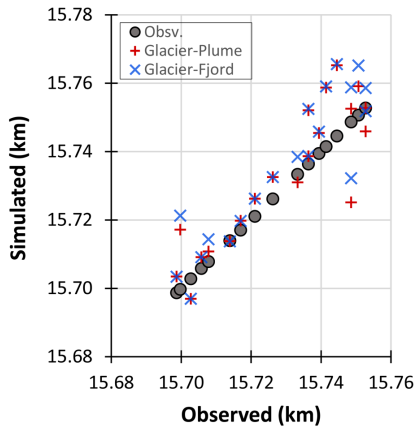

Figure 2.2.16 Model residuals. Simulated vs observed front positions (glacier length) of the best−fit configuration (Scenario 1 of submarine melting and factor $f = 75$ for crevasse water depth) resulting from the glacier−plume (red crosses) and the glacier−fjord (blue blades) models.

ICE DISCHARGE PARTITIONING: SUBMARINE MELTING + CALVING

Comparing the trends of cumulative calving and cumulative maximum submarine melting, we see a similar pattern for both models (Fig. 2.2.16). The curve follows a discontinuous increase, where the flat segments of the curve correspond to front advances subjected to submarine melting alone. The steps, on the other hand, represent episodes of calving. It seems that melting acts to undercut the front until the undercut section calves off. As described earlier, the first simulated front retreat corresponds to week 12 to 13, accounting for almost 20 (12) m of calved front in the glacier−plume (−fjord) model, when total maximum submarine melting of around 18 (10) m were already accumulated until that week. These ablation differences between both models become smaller towards the end of the simulation (when differences in the fjord boundary conditions between models are smaller). At the end of the 20−week simulation, the glacier−plume (−fjord) model accumulates total calving and maximum submarine melting of 94 (91) and 118 (108) m, respectively. These results give a 1:1.2 ratio of linear frontal ablation between the two mechanisms, calving and submarine melting, for both the glacier−plume and the glacier−fjord models. This ratio arises because at the end of the time series there has been a short period of melting but not calving, leaving the terminus undercut and primed for the next calving event. However, if measured immediately after the last calving event (week 19), the ratio would be much closer to 1:1, meaning that calving keeps pace with melting with no apparent multiplier effect.

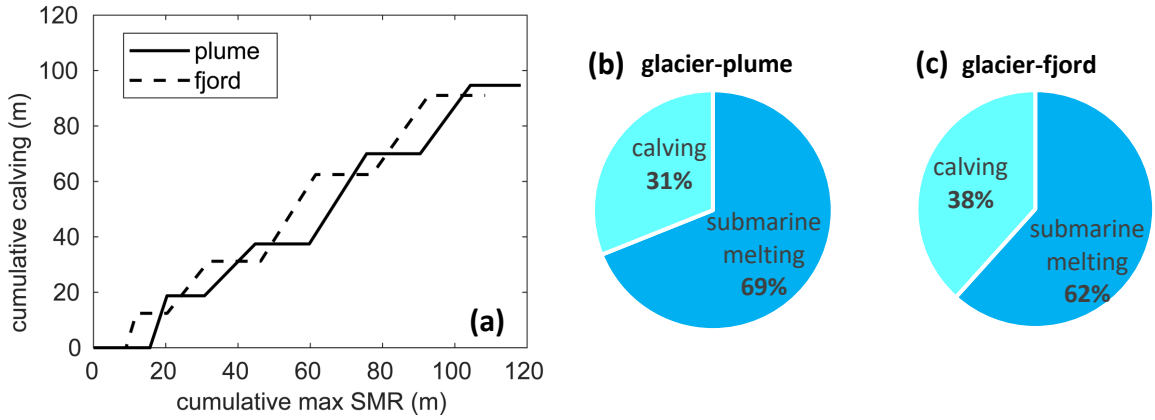

Figure 2.2.17 a) Comparison of cumulative calving against accumulation of maximum SMR resulting from glacier−plume (solid line) and glacier−fjord (dashed line) models along the simulation period. Note that the first simulated front retreat (calving > 0 m) corresponds to week 12 to 13 (Fig. 2.2.15g, h, i). Ice discharge partitioning into calving and submarine melting obtained from b) the glacier-plume and c) the glacier-fjord coupled models.

Given that we have the weekly submarine melt profiles (melt at all depths) and that calving always results in a vertical icefront, we can calculate the frontal ablation area lost by each mechanism and obtain the ice discharge partitioning for Hansbreen during the melt season of 2010 (Fig. 2.2.15b, c).

3. Synthesis on achievements concerning stakeholder needs and data gaps

The main needs by the stakeholders summarized at the end of Section 1.1 have been satisfied through the demonstration for stakeholders (both video and this accompanying written report) developed in the frames of INTAROS Deliverable 6.17. In particular:

- The GEUS solid ice discharge (https://dataverse01.geus.dk/dataverse/ice_discharge) and freshwater runoff (https://dataverse01.geus.dk/dataverse/freshwater) products, available through the INTAROS data portal and the GEUS dataverse repository provide, respectively, high spatial scale (glacier/basin scale) and high temporal resolution (12 days and 1 day, respectively) estimates of solid ice discharge and freshwater runoff from all of Greenland glaciers (limited, of course, to the marine-terminating ones in the case of solid ice discharge). Further information on these data products can be found in Mankoff et al. (2020a and 2002b, respectively).
- The modelling-based approach developed by UPM allows separating the contributions to solid ice discharge by its two main components, iceberg calving and submarine melting. In addition to this report and its accompanying videos (long and short versions, available through the INTAROS YouTube channel and the education material of the INTAROS website), further information on this modelling approach can be found in De Andrés et al. (2018, 2020, 2021).

The two most notable **gaps** detected are:

- **Data gaps:** Two main data gaps have been detected:
  - The GEUS solid ice discharge and freshwater runoff tools are available only for Greenland glaciers, but not for the rest of the Arctic. Having available similar data products for other Arctic regions, such as the Canadian Arctic, Svalbard and the Russian Arctic, would be most beneficial for e.g., getting updated estimates of contribution of mass losses from Arctic glaciers and ice sheets to sea-level rise. How to fill this data gap is further discussed in Chapter 4.
  - As The UPM modelling-based approach is very data demanding, it is not easy to find glacier-fjord systems for which the various required data are available. In the case study developed in Section 2.2.2 we saw that, even for an intensively monitored glacier-fjord system such as Hansbreen-Hansbutka, the necessary observations overlapped only over s very short period.
- **Modelling gaps:** The modelling-based approach developed by UPM to quantify the separation of solid ice discharge into iceberg calving and submarine melting shows the three following most notable limitations:
  - The operational version available is a two-dimensional model, although it allows for approximate three-dimensional estimates such as those described at the end of the video demonstration. The INTAROS UPM research team is currently working on overriding this limitation by developing a fully 3-D version of the coupled glacier-fjord/plume model.
  - It has been developed for tidewater glaciers, so it is not immediately applicable to floating tongues and ice shelves. This, however, is not an important limitation for the Arctic region, as such kind of floating ice bodies are rather scarce in the Arctic.

- It is extremely data-demanding, requiring a variety of data that are seldom available for many Arctic glaciers. Moreover, it does not use – as input – observational data such as the solid ice discharge available through the corresponding GEUS data product (the freshwater runoff from the GEUS product can, however, be readily incorporated as input data to the model). This is because the coupled glacier-fjord model computes by itself the amounts of iceberg calving and of submarine melt at the glacier front, whose sum is the solid ice discharge (assuming no front position changes; otherwise, they must be added). This, however, provides an independent data validation for the GEUS ice discharge product (or conversely). It would be useful, anyway, to develop a simpler procedure (first approach) to allow the partitioning of ice discharge into iceberg calving and submarine melting directly using the output from the GEUS solid ice discharge and freshwater runoff discharge products.

How to fill the above data and modelling gaps is further discussed in Chapter 4.

4. Outlook and recommendations for roadmap

The GEUS solid ice discharge and freshwater runoff products available through the INTAROS data portal and the GEUS Dataverse repository, as well as the UPM modelling-based approach to quantify the contributions of iceberg calving and submarine melting to solid ice discharge, have a large potential to estimate the current contributions of Arctic glaciers and ice sheets to sea-level rise, as well as gaining insight into the physical underlying processes, thus improving their prediction capability and leading to more accurate projections of sea-level rise under given greenhouse gasses emission scenarios.

The main recommendations for roadmap are linked to filling the data and modelling gaps described in the previous chapter. In particular:

- To develop products like the GEUS solid ice discharge and freshwater runoff products for Greenland for other Arctic regions, i.e., the Canadian Arctic, Svalbard, and the Russian Arctic. In a similar way as GEUS has assumed this responsibility for the Greenland ice sheet and its outlet glaciers, other research Institutions in Canada, Svalbard and Russia could take on the responsibility for such task regarding their corresponding Arctic territories. This would require a sustained investment, but would be most beneficial for getting improved and updates estimates of the contribution of Arctic glacier wastage to sea-level rise.
- To establish, as recommended in Deliverable 6.16, super sites where multi-disciplinary data are acquired, with the aim of overcoming the problem of the lack of observations co-located in time and space, as required e.g., by the UPM-developed model-based approach to separate the components of solid ice discharge.
- To improve the modelling-based approach developed by UPM, which separates solid ice discharge into iceberg calving and submarine melting, along the lines described below:
  - To create an operational fully three-dimensional version of the coupled glacier-fjord/plume model developed so far. This work is under way, and rather advanced, but will not be completed before the termination of the INTAROS project. Its completion, however, will be a notable legacy of INTAROS project.

- To extend the model, currently applicable to tidewater glaciers, to encompass floating tongues and ice shelves. The necessary changes would mostly affect to the glacier component of the coupled glacier-fjord/plume model and its finite-element gridding routine.
- To develop an alternative approach, based on a simpler model, capable to directly use as input, in addition to the GEUS freshwater runoff product results (the model already has this capability), the results generated by the GEUS ice discharge product, in such a way that the procedure could directly estimate the approximate partitioning of this discharge into iceberg calving and submarine melting. Such a quantification of the respective shares would be less exact than that produced by the currently available model (or its 3-D extension) but would be much less data demanding (in fact, the most critical data would be readily available) and much less computational-time consuming.

5. Summary

We here summarize the main aspects of Deliverable 6.17, with emphasis on its relation to other work packages, and individual tasks and deliverables of INTAROS project.

D6.17 is one of the outcomes of Task 6.4-Natural hazards in the Arctic, which is part of the Work Package 6-Applications of iAOS towards Stakeholders. This deliverable describes a modelling-based approach developed by UPM for the calculation of solid ice discharge as the sum of iceberg calving and submarine melting, so allowing the partitioning of ice discharge into its two main components, which is of much interest for the forecasting of the contribution of glacier wastage to sea-level rise. Note that sea-level rise, considered as a planetary-scale natural hazard, is one of the focal themes of Task 6.4-Natural hazards in the Arctic. Moreover, D6.17 provides a tool for validation of the observation-based estimates of ice discharge such as those provided by the solid ice discharge product developed by GEUS and introduced in D6.16 (Task 6.4), whose error can be estimated as described in its Section 4.3.4. The modelling approach is highly data-demanding, and hence it was conceived to be applied to selected Greenland and Svalbard glaciers. In particular, the coupled glacier dynamics-fjord circulation, and its alternative, simpler version glacier dynamics-buoyant plume model, have been applied to Hansbreen glacier-Hansbutka fjord system, in southern Svalbard. The plume parameterisation model was first tested for the Saqqarliup Sermia glacier- Saqqarleq fjord system, in central-western Greenland.

The coupled model can be fed, for subglacial discharge, by the output of the observation-based estimates of freshwater runoff provided by freshwater runoff product developed by GEUS and introduced in D6.16. Other typical input data to the model are:

- Glacier surface velocities (e.g. SAR remotely sensed velocities such as those provided by the European Space Agency (ESA) Sentinel-1 mission, available through the Copernicus Open Access Hub (https://scihub.copernicus.eu/).
- Glacier ice-thickness data such as those from the Glacier Thickness Database (GlaThiDa Consortium, 2020; Gärtner-Roer et al., 2014; Welty et al., 2020), maintained under the frameworks of the Global Terrestrial Network for Glaciers (GTN-G, https://www.gtn-g.ch/), jointly run by three operational bodies (the World Glacier Monitoring Service (WGMS), the US National Snow and Ice Data Center (NSIDC), and the Global Land Ice Measurements from Space (GLIMS) initiative) and hosted by WGMS (https://www.gtn-g.ch/glathida/).

- Surface mass balance data and glacier front position changes such as those available from the Global Glacier Change Bulletin (GGCB) series (WGMS, 2021b) and the Fluctuations of Glaciers (FoG) database (WGMS, 2021a) and browser hosted by the WGMS (http://wgms.ch/fogbrowser/).
- Glacier outlines from the Randolph Glacier Inventory (RGI Consortium, 2017), hosted by the National Snow and Ice Data Center (NSIDC) (https://www.glims.org/RGI/).

The latter three databases were among those assessed under various tasks, and associated deliverables of INTAROS WP2-Exploitation of existing observing systems, namely:

- Task 2.1 (Assessment of existing Arctic Observing Systems and identification of essential gaps relative to EAV and stakeholders needs) D2.7-Report on present observing capacities and gaps: Land and cryosphere.
- Task 2.2 (Exploitation of existing data towards improved data products) D2.8-Report on exploitation of existing data: Land and cryosphere.
- Task 2.4 (Synthesis and recommendations) D2.10-Synthesis of gap analysis and exploitation of the existing Arctic observing systems and D2.11-Report on the maturity of existing observing systems in the Arctic.

Moreover, ice-thickness data such as that stored in GlaThiDa database are collected by ground-penetrating radar (GPR) systems such as VIRL7 and VIRL8, the latter being an improvement of the former, developed by UPM under INTAROS Task 3.1-Coastal Greenland of WP3-Enhancement of multidisciplinary in situ observing systems. The corresponding information is part of deliverables:

- D3.1-Report on technical development and system design: Coastal Greenland
- D3.6-First implementation of the observing system: Data delivery and report on results of the observing systems in the coastal Greenland
- D3.10-Final implementation of the observing system: Data delivery and report on results of the observing systems in the coastal Greenland

The GEUS-developed solid ice discharge and freshwater products have been made accessible trough the INTAROS data portal, as part of Task 5.3-Integrate data from existing repositories into iAOS of WP5-Data integration and management.

The video demonstrations (long and short versions) generated as part of the present deliverable have been made available through the YouTube channel and the education material of the INTAROS website as part of Task 7.4-Interdisciplinary science dissemination of WP7-Dissemination and outreach.

Finally, the recommendations for Roadmap described in Chapter 4 will be used as input of D1.10-Roadmap for sustainable Arctic Observing System of WP1-Requirements and strategy for a Pan-Arctic system.

Literature

Adcroft, A., C. Hill, and J. Marshall, 1997: Representation of topography by shaved cells in a height coordinate ocean model. *Mon. Weather Rev.*, **125**, 2293–2315.

De Andrés, E., J. Otero, F. Navarro, A. Prominska, J. Lapazaran, and W. Walczowski, 2018: A two-dimensional glacier–fjord coupled model applied to estimate submarine melt rates and front position changes of Hansbreen, Svalbard. *J. Glaciol.*, **64**, 745–758, https://doi.org/10.1017/jog.2018.61.

De Andrés, E., D. Slater, F. Straneo, J. Otero, S. Das, and F. Navarro, 2020: Surface emergence of glacial plumes determined by fjord stratification. *Cryosphere*, 1–41, https://doi.org/10.5194/tc-2019-264.

Arakawa, A., and V. R. Lamb, 1977: Computational design of the basic dynamical processes of the UCLA general circulation model. *Methods Comput. Phys.*, **17**, 173–265.

Arthern, R. J., and G. H. Gudmundsson, 2010: Initialization of ice-sheet forecasts viewed as an inverse Robin problem. *J. Glaciol.*, **56**, 527–533, https://doi.org/10.3189/002214310792447699.

Bamber, J. L., A. J. Tedstone, M. D. King, I. M. Howat, E. M. Enderlin, M. R. van den Broeke, and B. Noel, 2018: Land Ice Freshwater Budget of the Arctic and North Atlantic Oceans: 1. Data, Methods, and Results. *J. Geophys. Res. Ocean.*, **123**, 1827–1837, https://doi.org/10.1002/2017JC013605.

Benn, D. I., N. R. J. Hulton, and R. H. Mottram, 2007: "Calving laws", "sliding laws" and the stability of tidewater glaciers. *Ann. Glaciol.*, **46**, 123–130, https://doi.org/10.3189/172756407782871161.

Blaszczyk, M., J. a Jania, and J. O. Hagen, 2009: Tidewater glaciers of Svalbard: Recent changes and estimates of calving fluxes. *Polish Polar Res.*, **30**, 85–142.

Borstad, C. P., A. Khazendar, E. Larour, M. Morlighem, E. Rignot, M. P. Schodlok, and H. Seroussi, 2012: A damage mechanics assessment of the Larsen B ice shelf prior to collapse: Toward a physically-based calving law. *Geophys. Res. Lett.*, **39**, 1–5, https://doi.org/10.1029/2012GL053317.

Carazzo, G., E. Kaminski, and S. Tait, 2006: The route to self-similarity in turbulent jets and plumes. *J. Fluid Mech.*, **547**, 137–148, https://doi.org/10.1017/S002211200500683X.

Carroll, D., D. A. Sutherland, E. L. Shroyer, J. D. Nash, G. A. Catania, and L. A. Stearns, 2015: Modelling Turbulent Subglacial Meltwater Plumes: Implications for Fjord-Scale Buoyancy-Driven Circulation. *J. Phys. Oceanogr.*, **45**, 2169–2185, https://doi.org/10.1175/JPO-D-15-0033.1.

Carroll, D., and Coauthors, 2016: The impact of glacier geometry on meltwater plume structure and submarine melt in Greenland fjords. *Geophys. Res. Lett.*, **43**, 9739–9748, https://doi.org/10.1002/2016GL070170.

Cowton, T., D. Slater, A. Sole, D. Goldberg, and P. Nienow, 2015: Modelling the impact of glacial runoff on fjord circulation and submarine melt rate using a new subgrid-scale parameterization for glacial plumes. *J. Geophys. Res. Ocean.*, **120**, 796–812, https://doi.org/10.1002/2014JC010324.

——, A. Sole, P. Nienow, D. Slater, D. Wilton, and E. Hanna, 2016: Controls on the transport of oceanic heat to Kangerdlugssuaq Glacier, East Greenland. *J. Glaciol.*, **62**, 1167–1180, https://doi.org/10.1017/jog.2016.117.

Csatho, B. M., A. F. Schenk, C. J. van der Veen, G. Babonis, K. Duncan, S. Rezvanbehbahani, M. R. van den Broeke, S. B. Simonsen, S. Nagarajan and J. H. van Angelen, 2014: Laser altimetry reveals complex pattern of Greenland Ice Sheet dynamics. *Proc. Natl. Acad. Sci.*, **111** (52) 18478–18483, https://doi.org/10.1073/pnas.1411680112.

Cuffey, K. M., and W. S. B. Paterson, 2010: *The Physics of Glaciers*. 4th ed. Elsevier, 704 pp.

Cushman-Roisin, B., and J.-M. Beckers, 2011: *Introduction to Geophysical Fluid Dynamics. Physical and Numerical Aspects*. 2nd ed. Academic Press.

De Andrés, E., J. Otero, F. Navarro, J. Promińska, J. Lapazaran and W. Walczowski, 2018:. A two-dimensional glacier–fjord coupled model applied to estimate submarine melt rates and front position changes of Hansbreen, Svalbard. *J. Glaciol.*, **64**(247), 745–758, https://doi.org/10.1017/jog.2018.61.

De Andrés, E. , D. A. Slater, F. Straneo, J. Otero, S. Das and F.J. Navarro, 2020:. Surface emergence of glacial plumes determined by fjord stratification. *Cryosphere*, **14**, 1951–1969. https://doi.org/10.5194/tc-14-1951-2020.

De Andrés, E., J. Otero, F. Navarro and W. Walczowsk, 2021: Glacier–plume or glacier–fjord circulation models? A 2-D comparison for Hansbreen–Hansbukta system, Svalbard. *J. Glaciol.*, **67**(265), 797–810, https://doi.org/10.1017/jog.2021.27.

Edwards, T. L., S. Nowicki, B. Marzeion, R. Hock, H. Goelzer, H. Seroussi, N. C. Jourdain, D. A. Slater, F. E. Turner, C. J. Smith, C. M. McKenna, E. Simon, A. Abe-Ouchi, J. M. Gregory, E. Larour, W. H. Lipscomb, A. J. Payne, A. Shepherd, C. Agosta, P. Alexander, T. Albrecht, B. Anderson, X. Asay-Davis, A. Aschwanden, A. Barthel, A. Bliss, R. Calov, R., C. Chambers, N. Champollion, Y. Choi, R. Cullather, J. Cuzzone, C. Dumas, D. Felikson, X. Fettweis, K. Fujita, B. K. Galton-Fenzi, R. Gladstone, N. R. Golledge, R. Greve, T. Hattermann, M. J. Hoffman, A. Humbert, M. Huss, P. Huybrechts, Immerzeel, T. Kleiner, P. Kraaijenbrink, S. Le clec'h, V. Lee, G. R. Leguy, C. M. Little, D. P. Lowry, J. H. Malles, D. F. Martin, F. Maussion, M. Morlighem, J. F. O'Neill, I. Nias, F. Pattyn, T. Pelle, S. F. Price, A. Quiquet, V. Radić, R. Reese, D. R. Rounce, M. Rückamp, M., A. Sakai, C. Shafer, N. J. Schlegel, S. Shannon, R. S. Smith, F. Straneo, S. Sun, L. Tarasov, L. D. Trusel, J. van Breedam, R. van de Wal, M. van den Broeke, R. Winkelmann, H. Zekollari, C. Zhao, T. Zhang and T. Zwinger, 2021: Projected Land Ice Contributions to Twenty-First-Century Sea Level Rise. *Nature*, **593** (7857), 74–82. https://doi.org/10.1038/s41586-021-03302-y.

Enderlin, E.M., I.M. Howat, S. Jeong, M.-J. Noh, J.H. van Angelen and M.R. van den Broeke, 2014: An improved mass budget for the Greenland ice sheet. *Geophys. Res. Lett.*, **41**, 866–872, https://doi.org/10.1002/2013GL059010.

Fettweis, X., S. Hofer, U. Krebs-Kanzow, C. Amory, T. Aoki, C. J. Berends, A. Born, J. E. Box, A. Delhasse, K. Fujita, P. Gierz, H. Goelzer, E. Hanna, A. Hashimoto, P. Huybrechts, M.-L. Kapsch, M. D. King, C. Kittel, C. Lang, P. L. Langen, , J. T. M. Lenaerts, G. E. Liston, G. Lohmann, S. H. Mernild, U. Mikolajewicz, K. Modali, R. H. Mottram, M. Niwano, B. Noël, J. C. Ryan, A. Smith, J. Streffing, M. Tedesco, W. J. van de Berg, M. van den Broeke, R. S. W. van de Wal, L. van Kampenhout, D. Wilton, B. Wouters, F. Ziemen and T. Zolles, 2020: GrSMBMIP: intercomparison of the modelled 1980–2012 surface mass balance over the Greenland Ice Sheet. *The Cryosphere*, **14**(11), 3935–3958, https://doi.org/10.5194/tc-14-3935-2020.

Finkelnburg, R., 2013: Climate variability of Svalbard in the first decade of the 21st century and its impact on Vestfonna ice cap, Nordaustlandet. Technische Universität Berlin, 205 pp.

Fried, M. J., and Coauthors, 2015: Distributed subglacial discharge drives significant submarine melt at a Greenland tidewater glacier. *Geophys. Res. Lett.*, **42**, 9328–9336, https://doi.org/10.1002/2015GL065806.

Gagliardini, O., and Coauthors, 2013: Capabilities and performance of Elmer/Ice, a new-generation ice sheet model. *Geosci. Model Dev.*, **6**, 1299–1318, https://doi.org/10.5194/gmd-6-1299-2013.

Gärtner-Roer, I., K. Naegeli, M. Huss, T. Knecht, H. Machguth and M. Zemp, 2014: A database of worldwide glacier thickness observations. *Global Planet. Change*, **122**, 330–344, https://doi.org/10.1016/j.gloplacha.2014.09.003.

GlaThiDa Consortium, 2020: *Glacier Thickness Database* 3.1.0. World Glacier Monitoring Service, Zurich, Switzerland. DOI: 10.5904/wgms-glathida-2020-10

Glen, J. W., 1955: The creep of polycrystalline ice. *Cold Reg. Sci. Technol.*, **11**, 285–300, https://doi.org/10.1016/0165-232X(85)90052-7.

Grabiec, M., J. Jania, D. Puczko, L. Kolondra, and T. Budzik, 2012: Surface and bed morphology of Hansbreen, a tidewater glacier in Spitsbergen. *Polish Polar Res.*, **33**, 111–138, https://doi.org/10.2478/v10183-012-0010-7.

Hanna, E., and Coauthors, 2020: Mass balance of the ice sheets and glaciers – Progress since AR5 and challenges. *Earth-Science Rev.*, **201**, 102976, https://doi.org/10.1016/j.earscirev.2019.102976.

Holland, D. M., and A. Jenkins, 1999: Modelling Thermodynamic Ice–Ocean Interactions at the Base of an Ice Shelf. *J. Phys. Oceanogr.*, **29**, 1787–1800, https://doi.org/10.1175/1520-0485(1999)029<1787:MTIOIA>2.0.CO;2.

Holmes, F. A., N. Kirchner, J. Kuttenkeuler, J. Krützfeldt, and R. Noormets, 2019: Relating ocean temperatures to frontal ablation rates at Svalbard tidewater glaciers: Insights from glacier proximal datasets. *Sci. Rep.*, **9**, 9442, https://doi.org/10.1038/s41598-019-45077-3.

Hopwood, M. J., D. Carroll, T. J. Browning, L. Meire, J. Mortensen, S. Krisch, and E. P. Achterberg, 2018: Non-linear response of summertime marine productivity to increased meltwater discharge around Greenland. *Nat. Commun.*, **9**, 3256, https://doi.org/10.1038/s41467-018-05488-8.

Hugonnet, R., B. McNabb, E. Berthier, B Menounos, C. Nuth, L. Girod, D. Farinotti, M. Huss, I. Dussaillant, F. Brun and A. Kääb, 2021: Accelerated Global Glacier Mass Loss in the Early Twenty-First Century. *Nature*, **592**(7856), 726–731, https://doi.org/10.1038/s41586-021-03436-z.

Huss, M., and R. Hock, 2015: A new model for global glacier change and sea-level rise. *Front. Earth Sci.*, **3**, 1–22, https://doi.org/10.3389/feart.2015.00054.

IPCC, 2019: Technical Summary. *IPCC Special Report on the Ocean and Cryosphere in a Changing Climate*, H.-O. Pörtner et al., Eds., In press., 35–74.

Jackett, D. R., and T. J. Mcdougall, 1995: Minimal Adjustment of Hydrographic Profiles to Achieve Static Stability. *J. Atmos. Ocean. Technol.*, **12**, 381–389, https://doi.org/10.1175/1520-0426(1995)012<0381:MAOHPT>2.0.CO;2.

Jackson, R. H., and Coauthors, 2017: Near-glacier surveying of a subglacial discharge plume: Implications for plume parameterizations. *Geophys. Res. Lett.*, **44**, 6886–6894, https://doi.org/10.1002/2017GL073602.

Jay-Allemand, M., F. Gillet-Chaulet, O. Gagliardini, and M. Nodet, 2011: Investigating changes in basal conditions of Variegated Glacier prior to and during its 1982–1983 surge. *Cryosphere*, **5**, 659–672, https://doi.org/10.5194/tc-5-659-2011.

Jenkins, A., 2011: Convection-Driven Melting near the Grounding Lines of Ice Shelves and Tidewater Glaciers. *J. Phys. Oceanogr.*, **41**, 2279–2294, https://doi.org/10.1175/JPO-D-11-03.1.

——, K. W. Nicholls, and H. F. J. Corr, 2010: Observation and Parameterization of Ablation at the Base of Ronne Ice Shelf, Antarctica. *J. Phys. Oceanogr.*, **40**, 2298–2312, https://doi.org/10.1175/2010JPO4317.1.

Kaminski, E., S. Tait, and G. Carazzo, 2005: Turbulent entrainment in jets with arbitrary buoyancy. *J. Fluid Mech.*, **526**, 361–376, https://doi.org/10.1017/S0022112004003209.

Krug, J., J. Weiss, O. Gagliardini, and G. Durand, 2014: Combining damage and fracture mechanics to model calving. *Cryosphere*, **8**, 2101–2117, https://doi.org/10.5194/tc-8-2101-2014.

Krug, J., G. Durand, O. Gagliardini, and J. Weiss, 2015: Modelling the impact of submarine frontal melting and ice mélange on glacier dynamics. *Cryosphere*, **9**, 989–1003, https://doi.org/10.5194/tc-9-989-2015.

Langen, P. L., R. S. Fausto , B. Vandecrux, R. H. Mottram and J. E. Box, 2017: Liquid Water Flow and Retention on the Greenland Ice Sheet in the Regional Climate Model HIRHAM5: Local and Large-Scale Impacts. *Front. Earth Sci.*, **4**, 110, https://doi.org/10.3389/feart.2016.00110.

Luckman, A., D. I. Benn, F. Cottier, S. Bevan, F. Nilsen, and M. Inall, 2015: Calving rates at tidewater glaciers vary strongly with ocean temperature. *Nat. Commun.*, **6**, 8566, https://doi.org/10.1038/ncomms9566.

Mankoff, K. D., F. Straneo, C. Cenedese, S. B. Das, C. G. Richards, and H. Singh, 2016: Structure and dynamics of a subglacial discharge plume in a Greenlandic fjord. *J. Geophys. Res. Ocean.*, **121**, 8670–8688, https://doi.org/10.1002/2016JC011764.

Mankoff, K. D., A. Solgaard, W. Colgan, William, A. P. Ahlstrøm, S. A. Khan and R. S. Fausto, 2020a: Greenland Ice Sheet solid ice discharge from 1986 through March 2020. *Earth System Sci. Data*, **12**(2), 1367–1383, https://doi.org/10.5194/essd-12-1367-2020.

Mankoff, K. D., B. Noël, X. Fettweis, A. P. Ahlstrøm, W. Colgan, K. Kondo, K. Langley, Kirsty, S. Sugiyama, D. van As and R. S. Fausto, 2020b: Greenland liquid water discharge from 1958 through 2019. *Earth System Sci. Data*, **12**(4), 2811–2841, https://doi.org/10.5194/essd-12-2811-2020.

Marshall, J., A. Adcroft, C. Hill, L. Perelman, and C. Heisey, 1997a: A finite-volume, incompressible Navier Stokes model for studies of the ocean on parallel computers. *J. Geophys. Res. Ocean.*, **102**, 5753–5766, https://doi.org/10.1029/96JC02775.

——, C. Hill, L. Perelman, and A. Adcroft, 1997b: Hydrostatic, quasi-hydrostatic, and nonhydrostatic ocean modelling. *J. Geophys. Res. Ocean.*, **102**, 5733–5752, https://doi.org/10.1029/96JC02776.

McDougall, T. J., and P. M. Barker, 2011: *Getting started with TEO-10 and the Gibbs Seawarer Oceanographic Toolbox*. SCOR/IAPSO WG127, Ed. 28 pp.

Meire, L., and Coauthors, 2015: Glacial meltwater and primary production are drivers of strong CO2 uptake in fjord and coastal waters adjacent to the Greenland Ice Sheet. *Biogeosciences*, **12**, 2347–2363, https://doi.org/10.5194/bg-12-2347-2015.

Meire, L., and Coauthors, 2017: Marine-terminating glaciers sustain high productivity in Greenland fjords. *Glob. Chang. Biol.*, **23**, 5344–5357, https://doi.org/10.1111/gcb.13801.

Morlighem, M., C. N. Williams, E. Rignot, L. An, J. E. Arndt, J. L.Bamber, G. Catania, N. Chauché, J. A. Dowdeswell, B. Dorschel, I. Fenty, K. Hogan, K., I. M. Howat, A. Hubbard, M. Jakobsson, T. M. Jordan, K. K. Kjeldsen, R. Millan, L. Mayer, J. Mouginot, B. P. Y. Noël, C. Ó. Cofaigh, S. Palmer, S. Rysgaard, H. Seroussi, M. J. Siegert, P. Slabon, F. Straneo, M. R. van den Broeke, W. Weinrebe, M. Wood and K. B. Zinglersen, 2017: BedMachine v3: Complete bed topography and ocean bathymetry mapping of Greenland from multi-beam echo sounding combined with mass conservation. *Geophys. Res. Lett*, **44**(21), 11051–11061, https://doi.org/10.1002/2017GL074954.

Motyka, R. J., W. P. Dryer, J. Amundson, M. Truffer, and M. Fahnestock, 2013: Rapid submarine melting driven by subglacial discharge, LeConte Glacier, Alaska. *Geophys. Res. Lett.*, **40**, 5153–5158, https://doi.org/10.1002/grl.51011.

Mugford, R. I., and J. A. Dowdeswell, 2011: Modelling glacial meltwater plume dynamics and sedimentation in high-latitude fjords. *J. Geophys. Res. Earth Surf.*, **116**, n/a-n/a, https://doi.org/10.1029/2010JF001735.

Navarro, F. J., A. Martín-Español, J. J. Lapazaran, M. Grabiec, J. Otero, E. V Vasilenko, and D. Puczko, 2014: Ice Volume Estimates from Ground-Penetrating Radar Surveys, Wedel Jarlsberg Land Glaciers, Svalbard. *Arctic, Antarct. Alp. Res.*, **46**, 394–406, https://doi.org/10.1657/1938-4246-46.2.394.

Nye, J. F., 1957: The Distribution of Stress and Velocity in Glaciers and Ice-Sheets. *Proc. R. Soc. A Math. Phys. Eng. Sci.*, **239**, 113–133, https://doi.org/10.1098/rspa.1957.0026.

——, 1965: The Flow of a Glacier in a Channel of Rectangular, Elliptic or Parabolic Cross-Section. *J. Glaciol.*, **5**, 661–690, https://doi.org/10.3189/s0022143000018670.

Oliver, H., and Coauthors, 2018: Exploring the Potential Impact of Greenland Meltwater on Stratification, Photosynthetically Active Radiation, and Primary Production in the Labrador Sea. *J. Geophys. Res. Ocean.*, **123**, 2570–2591, https://doi.org/10.1002/2018JC013802.

Otero, J., F. J. Navarro, C. Martin, M. L. Cuadrado, and M. I. Corcuera, 2010: A three-dimensional calving model: numerical experiments on Johnsons Glacier, Livingston Island, Antarctica. *J. Glaciol.*, **56**, 200–214, https://doi.org/10.3189/002214310791968539.

——, F. J. Navarro, J. J. Lapazaran, E. Welty, D. Puczko, and R. Finkelnburg, 2017: Modelling the Controls on the Front Position of a Tidewater Glacier in Svalbard. *Front. Earth Sci.*, **5**, 29, https://doi.org/10.3389/feart.2017.00029.

Overeem, I., B. D. Hudson, J. P. M. Syvitski, A. B. Mikkelsen, B. Hasholt, M. R. van den Broeke, B. P. Y. Noël, and M. Morlighem, 2017: Substantial export of suspended sediment to the global oceans from glacial erosion in Greenland. *Nat. Geosci.*, **10**, 859–863, https://doi.org/10.1038/ngeo3046.

Porter, C., P. Morin, I. Howat, M.-J. Noh, B. Bates, K. Peterman, S. Keesey, M. Schlenk, J. Gardiner, K. Tomko, M. Willis, C. Kelleher, M. Cloutier, E. Husby, S. Foga, Steven, H. Nakamura, M. Platson, Jr. Wethington, C. Williamson, G. Bauer, J. Enos, G. Arnold, W. Kramer, P. Becker, A. Doshi, C. D'Souza, P. Cummens, F. Laurier and M. Bojesen, 2018: *ArcticDEM, Harvard Dataverse V1*, 2018, Date accessed: 2019-11-14.

Puczko, D., 2012: Czasowa i przestrzenna zmienność ruchu spitsbergeńskich lodowców uchodzących do morza na przykładzie lodowca hansa. Polskiej Akademii Nauk, 143 pp.

RGI Consortium, 2017: *Randolph Glacier Inventory – A Dataset of Global Glacier Outlines*: Version 6.0: Technical Report, Global Land Ice Measurements from Space, Colorado, USA. Digital Media, https://doi.org/10.7265/N5-RGI-60.

Rignot, E., M. Koppes, and I. Velicogna, 2010: Rapid submarine melting of the calving faces of West Greenland glaciers. *Nat. Geosci.*, **3**, 187–191, https://doi.org/10.1038/ngeo765.

Sánchez-Gámez, P. and F.J. Navarro, 2018: Ice discharge error estimates using different cross-sectional area approaches: a case study for the Canadian High Arctic, 2016/17. *J. Glaciol*., **64**(246), 595–608, https://doi.org/10.1017/jog.2018.48.

Schild, K. M., and Coauthors, 2018: Glacier Calving Rates Due to Subglacial Discharge, Fjord Circulation, and Free Convection. *J. Geophys. Res. Earth Surf.*, **123**, 2189–2204, https://doi.org/10.1029/2017JF004520.

Sciascia, R., F. Straneo, C. Cenedese, and P. Heimbach, 2013: Seasonal variability of submarine melt rate and circulation in an East Greenland fjord. *J. Geophys. Res. Ocean.*, **118**, 2492–2506, https://doi.org/10.1002/jgrc.20142.

Seroussi, H., Y. Nakayama, E. Larour, D. Menemenlis, M. Morlighem, E. Rignot, and A. Khazendar, 2017: Continued retreat of Thwaites Glacier, West Antarctica, controlled by bed topography and ocean circulation. *Geophys. Res. Lett.*, **44**, 6191–6199, https://doi.org/10.1002/2017GL072910.

Slater, D., P. Nienow, A. Sole, T. Cowton, R. Mottram, P. Langen, and D. Mair, 2017: Spatially distributed runoff at the grounding line of a large Greenlandic tidewater glacier inferred from plume modelling. *J. Glaciol.*, **63**, 309–323, https://doi.org/10.1017/jog.2016.139.

Slater, D. A., P. W. Nienow, T. R. Cowton, D. N. Goldberg, and A. J. Sole, 2015: Effect of near-terminus subglacial hydrology on tidewater glacier submarine melt rates. *Geophys. Res. Lett.*, **42**, 2861–2868, https://doi.org/10.1002/2014GL062494.

Slater, D. A., D. N. Goldberg, P. W. Nienow, and T. R. Cowton, 2016: Scalings for Submarine Melting at Tidewater Glaciers from Buoyant Plume Theory. *J. Phys. Oceanogr.*, **46**, 1839–1855, https://doi.org/10.1175/JPO-D-15-0132.1.

Solgaard, A, A. Kusk, J. P. Merryman Boncori, J. Dall, K. D. Mankoff, A. P. Ahlstrøm, S. B. Andersen, M. Citterio, N. B. Karlsson, K. K. Kjeldsen, N. J. Korsgaard, S. H. Larsen and R. S. Fausto, 2021: Greenland ice velocity maps from the PROMICE project. *Earth System Sci. Data*, **13**(7), 3491–3512, https:// doi.org/10.5194/essd-13-3491-2021.

Stevens, L. A., F. Straneo, S. B. Das, A. J. Plueddemann, A. L. Kukulya, and M. Morlighem, 2016: Linking glacially modified waters to catchment-scale subglacial discharge using autonomous underwater vehicle observations. *Cryosphere*, **10**, 417–432, https://doi.org/10.5194/tc-10-417-2016.

Straneo, F., and P. Heimbach, 2013: North Atlantic warming and the retreat of Greenland's outlet glaciers. *Nature*, **504**, 36–43, https://doi.org/10.1038/nature12854.

Todd, J., and P. Christoffersen, 2014: Are seasonal calving dynamics forced by buttressing from ice mélange or undercutting by melting? Outcomes from full-Stokes simulations of Store Glacier, West Greenland. *Cryosphere*, **8**, 2353–2365, https://doi.org/10.5194/tc-8-2353-2014.

van den Broeke, M.R., E. M. Enderlin, I. M. Howat, P. K. Munneke, B. P. Y. Noël, W. J. van de Berg, E. van Meijgaard and B. Wouters, 2016: On the recent contribution of the Greenland ice sheet to sea level change. *Cryosphere*, **10**, 1933–1946, https://doi.org/10.5194/tc-10-1933-2016.

Vieli, A., J. Jania, and L. Kolondra, 2002: The retreat of a tidewater glacier: observations and model calculations on Hansbreen, Spitsbergen. *J. Glaciol.*, **48**, 592–600, https://doi.org/10.3189/172756502781831089.

Welty, E., M. Zemp, F. Navarro, M. Huss, J.J. Fürst, I. Gärtner-Roer, J. Landmann, H. Machguth, K. Naegeli, L. M. Andreassen, D. Farinotti, H. Li and GlaThiDa Contributors, 2020: Worldwide version-controlled database of glacier thickness observations. *Earth Syst. Sci. Data*, **12**, 3039–3055**,** https://doi.org/10.5194/essd-2020-87.

WGMS, 2021a: *Fluctuations of Glaciers Database*. World Glacier Monitoring Service, Zurich, Switzerland, http://dx.doi.org/10.5904/wgms-fog-2021-05.

WGMS 2021b: *Global Glacier Change Bulletin* No. 4 (2018-2019). Zemp, M., Nussbaumer, S.U., Gärtner-Roer, I., Bannwart, J., Paul, F., and Hoelzle, M. (eds.), ISC(WDS)/IUGG(IACS)/UNEP/UNESCO/WMO, World Glacier Monitoring Service, Zurich, Switzerland, 278 pp., based on database version http://dx.doi.org/10.5904/wgms-fog-2021-05.

Xu, Y., E. Rignot, D. Menemenlis, and M. Koppes, 2012: Numerical experiments on subaqueous melting of Greenland tidewater glaciers in response to ocean warming and enhanced subglacial discharge. *Ann. Glaciol.*, **53**, 229–234, https://doi.org/10.3189/2012AoG60A139.

——, ——, I. Fenty, D. Menemenlis, and M. M. Flexas, 2013: Subaqueous melting of Store Glacier, west Greenland from three-dimensional, high-resolution numerical modelling and ocean observations. *Geophys. Res. Lett.*, **40**, 4648–4653, https://doi.org/10.1002/grl.50825.

Zemp, M.; M. Huss, E. Thibert, N. Eckert, R. McNabb, J. Huber, M. Barandun, H. Machguth, S. U. Nussbaumer, I. Gärtner-Roer, L. Thomson, F. Paul, F. Maussion, S. Kutuzov and J. G. Cogley, 2019: Global Glacier Mass Changes and Their Contributions to Sea-Level Rise from 1961 to 2016. *Nature*, **568**(7752), 382–386. https://doi.org/10.1038/s41586-019-1071-0.

---------- END of DOCUMENT----------

INTAROS

This report is made under the project

Integrated Arctic Observation System (INTAROS)

funded by the European Commission Horizon 2020 program

Grant Agreement no. 727890.

Project partners: